Computational fluid-structure interaction of a restrained ogive-cylindrical body with a blunt elliptical base at a high incidence

Mark Ishay ⊙, Oded Gottlieb ⊙, and David Degani ⊙
Department of Mechanical Engineering, Technion-Israel Institute of Technology, Haifa, Israel

The flow around an inclined tangent ogive-cylindrical body of a finite length with a blunt elliptical base, placed in a wind tunnel and allowed to yaw in the *x-y* plane, is studied computationally. The flow is three-dimensional, compressible, and laminar with a Reynolds number of 30 000 based on the body diameter and a Mach number of 0.2. The study covers the range of angles of attack from 0° to 65°, both for fixed and yaw-restrained configurations where solutions are determined after removal of initial disturbances. The flow around the fixed body, for $\alpha > 52°$ and after disturbance removal, is nonstationary with large amplitude oscillations; for $0° < \alpha < 52°$ the flow is almost steady with small nonstationary amplitude oscillations possibly due to the body's blunt end nonstationary wake. We identify a transition region between $45° < \alpha < 52°$ where the attached wake behind the body end becomes detached. The resulting yaw response exhibits an intricate bifurcation structure that includes bistable periodic (finite amplitude) and nonstationary (small amplitude) limit cycles for moderate angles of attack, and nonstationary (finite amplitude) oscillations for high angles of attack. Investigation of the restraint torsion stiffness reveals a resonant periodic lock-in phenomena for low angles of attack which becomes quasiperiodic for a 40° angle of attack.

I. INTRODUCTION

The flow around a pointed slender body of revolution at high incidence, despite the simplicity of the body geometry, is intricate and can generate significant side forces. The flow field can be so unstable that even upcoming turbulence [1] or a small upstream disturbance [2] can change the flow abruptly as demonstrated by the phantom yaw effect on maneuvering slender bodies [3]. It has been shown that these side forces can be altered by placing small irregularities near the body tip [2–5].

When such a slender-body model is mounted on a balance in a wind tunnel, the nonlinear interaction between the flow and the structure can play a significant role in the stability of the configuration, and therefore, in the accuracy of the measurements. A numerical investigation of the fluid-structure interaction taking into account the elastic effects of the restraint has revealed the existence of periodic and nonstationary oscillations for moderate and large angles of attack [4], culminating with an intricate bifurcation structure that included coexisting quasiperiodic tori and chaotic solutions foliated with periodic ultra-subharmonics [5]. Reference [6] described the study of a free-to-roll slender rigid body of revolution placed in a wind tunnel at a high angle of attack (AOA) where the resistance to the roll moment was represented by a linear torsion spring and equivalent linear damping represented friction in the bearings of a simulated wind tunnel model. The numerical investigation revealed bistable periodic limit-cycle oscillations, which lost their periodicity with increasing stiffness of the restraining spring.

In the past, most works investigating the flows around slender bodies at high angles of attack ignored the body's end effect on the flow instabilities, concentrating only on the forebody's effect

(e.g., Ref. [2]). When taken into account, the body was very long and the base flow had no, or little, effect on the flow at the front of the body (e.g., Ref. [7] where no details are given about incorporation of viscous effects). Sometime a sting is added; for example, Ref. [8] added a long (11D) sting but effect of the cylinder-sting junction was not investigated.

It is noteworthy that different end conditions have been found to effect both the downstream wake and consequent flow-induced vibration of elastically restrained cylinders [9] and recently the response of a restrained D-section cylinder with variable AOA [10]. Furthermore, experimental [11,12] studies have demonstrated the existence of asymmetric flow for slender body configurations mounted on rigid supports, whereas analytical [13] and computational [14] studies revealed stability of symmetric and asymmetric vortex pairs over a slender conical body. A recent experimental investigation of a cylindrical square-backed body with an elliptical-nose culminated with extensive leading-edge separation that led to significant wake asymmetry [15]. However, to-date the combined effects of slender bodies with a tangent shape ogive forebody nose and a blunt elliptical base have not been documented.

In the current research we numerically investigate a configuration where an inclined three-dimensional rigid tangent ogive-cylindrical body with a blunt elliptical base is mounted on a torsion spring and is allowed only to yaw. We focus on the self-excited dynamics describing the body's motion, and the resulting wake pattern. Since the body is short, the geometry of the body's end is important and its effect is also studied. The body is subjected to three-dimensional, compressible, laminar flow with a Reynolds number of 30 000 based on body diameter and Mach number of 0.2. The second-order implicit beam-warming finite-difference scheme is employed to solve the full Navier-Stokes equations, whereas the coupled structural equation is solved by an explicit fourth-order Runge-Kutta method. We employ a subiteration procedure for the flow-structure coupling.

II. PROBLEM FORMULATION

This section includes a summary of governing nondimensional equations and numerical algorithms for both the flow field (Sec. II A) and structure (Sec. II B) that are derived and described in great detail in previously published papers [4–6,16–21]. The numerical flow-structure coupling algorithm is subsequently summarized (Sec. II C), and we conclude with a detailed description of algorithm validation and verification (Sec. II D).

A. Flow field: Governing equations and numerical algorithm

The conservation equations of mass, momentum, and energy can be represented in a flux-vector form as

$$\partial_\tau \hat{Q} + \partial_\xi \hat{E} + \partial_\eta \hat{F} + \partial_\zeta \hat{G} = \frac{1}{\text{Re}}(\partial_\xi \hat{E}_\nu + \partial_\eta \hat{F}_\nu + \partial_\zeta \hat{G}_\nu), \tag{1}$$

where τ is the dimensionless time, $\tau = a_\infty t / D$, and the independent spatial variables ξ, η, and ς are chosen to map a curvilinear body-conforming grid into a uniform computational space. In Eq. (1), $\hat{Q}$ is the vector of dependent flow variables, $\hat{E} = \hat{E}(\hat{Q})$, $\hat{F} = \hat{F}(\hat{Q})$ and $\hat{G} = \hat{G}(\hat{Q})$ are the inviscid flux vectors, and the terms $\hat{E}_\nu$, $\hat{F}_\nu$, and $\hat{G}_\nu$ are fluxes containing derivatives of the viscous terms. A dimensionless form of the equations [16] is used throughout this work. The implicit beam-warming finite difference algorithm [17], which is second-order accurate both in time and space [18,19], is adapted to solve Eq. (1) in a three-dimensional curvilinear coordinate system [20], where all viscous terms are retained [21].

Computations were performed for subsonic flows over an ogive-cylinder body of diameter D, which consists of 3.5-diameter tangent ogive forebody with a 6.5-diameter cylindrical afterbody and blunt elliptic base (see Fig. 1). An adiabatic no-slip boundary condition was applied at the body surface implicit periodic continuation condition was imposed at the circumferential edges of the grid and undisturbed freestream conditions were maintained at the computational outer boundary.
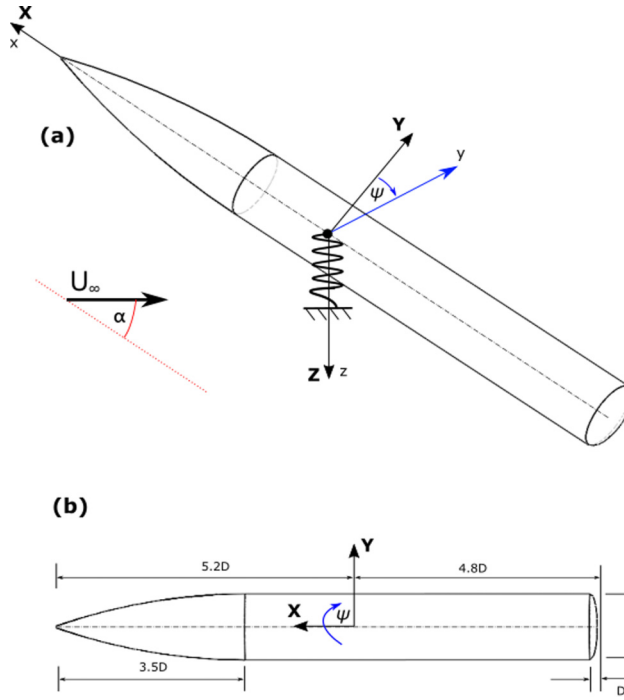
FIG. 1. Body and coordinate system (a) and top-view (b) of a tangent 3.5-diameter forebody, a 6.5-diameter cylindrical afterbody and blunt elliptic base. The slender body is mounted on a hinge-mounted torsion spring placed at 5.2-diameter that restricts motion to yaw and prevents pitch and roll.

The AOA α between the horizontal (X) and the free stream velocity (U_∞) was varied between zero and $65°$.

The grid consisted of 200 equispaced circumferential planes extending completely around the body. In each circumferential plane, the grid contained 60 radial points between the body surface and the computational outer boundary and 104 axial points between the nose and the rear of the body (see Fig. 2). In order to prevent asymmetries, the grid was created by rotating the two-dimensional (2D) leeside grid plane around the first quarter of the body, then, reflected to create the lower quarter and finally reflected left–right to make the full grid. The grid spacing was found adequate for resolving both the boundary-layer flow and the leeward vortices.

A small disturbance was placed near the tip and its height in all cases was set to $h/D = 0.004$. For each AOA at least three different disturbance locations were calculated; at circumferential angle $\Phi \sim 2°$ off the leeward plane of symmetry, at $\Phi = 90°$, i.e., perpendicular to windward plane of symmetry and at $\Phi \sim 176°$. In all cases presented (unless otherwise mentioned) the computations started from a uniform flow field and time-accurate computations were carried out. To obtain solutions after disturbance removal, the computations were carried out with a disturbance for 300 nondimensional time units and then the disturbance was removed and computations continued.

B. Structure: Governing equation and numerical algorithm

The ogive-cylinder body is considered rigid and is only allowed to yaw (in the x-y plane). The resistance to the yaw is represented by a linear torsion spring and linear equivalent damping simulating friction in the bearings. We make use of an Euler angle formulation [22] where the generalized coordinates (see Fig. 1) are defined in for pitch, yaw, and roll respectively: $q_j = (\theta, \psi, \phi)$. We limit the body to move only in the yaw (ψ) direction (i.e., $\theta = \phi = 0$) and obtain the following equation
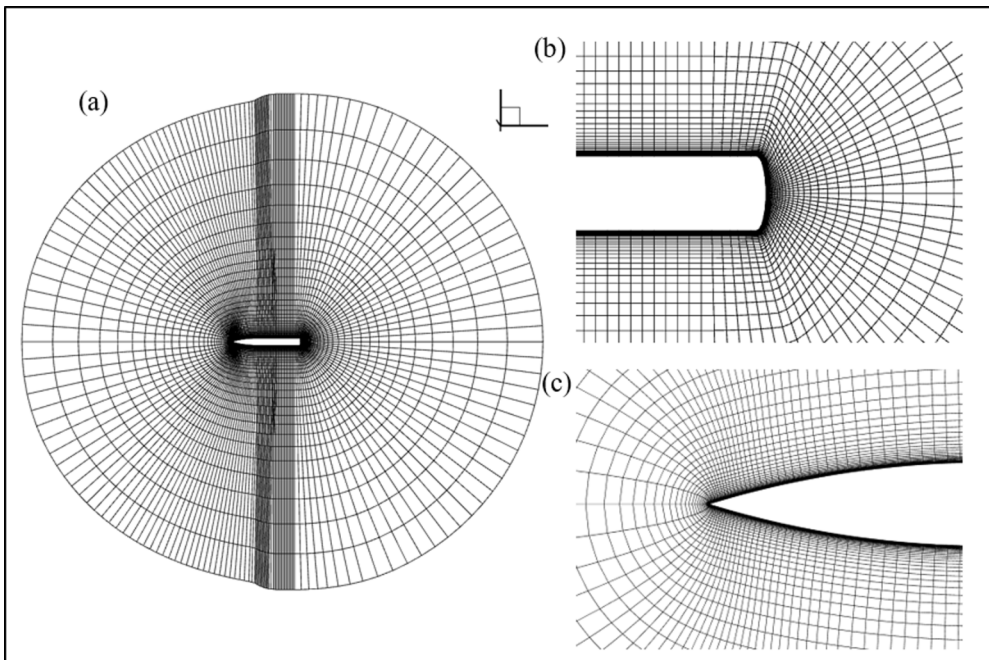
FIG. 2. Computational grid (a) and zoom-in on the body's blunt end (b) and on the ogive forebody (c). The grid consisted of 200 equispaced circumferential planes extending completely around the body. In each circumferential plane, the grid contained 60 radial points between the body surface and the computational outer boundary and 104 axial points between the nose and the end of the body.

for $\psi_{\tau\tau}$ (see Ref. [5]):

$$\psi_{\tau\tau} = -d_\psi \psi_\tau - k_\psi \psi + \mu C_\psi, \tag{2}$$

where C_ψ is the yaw aerodynamic moment.

The torsion stiffness and damping coefficients in the ψ direction (K_ψ and D_ψ, respectively) are normalized by the body moment of inertia I_{yy}, free stream speed of sound a_∞ and the body diameter D. The dimensionless parameter groups therefore are defined as

$$k_\psi = \frac{K_\psi}{a_\infty^2 D^{-2} I_{yy}}, \quad d_\psi = \frac{D_\psi}{a_\infty D^{-1} I_{yy}}, \quad \mu = \frac{\rho_\infty D^5 M_\infty^2}{2 I_{yy}}, \tag{3}$$

where μ is the mass ratio and M_∞ is the free stream Mach number.

Linearization of the equation of motion enables computation of the dynamical system natural frequency ($\omega_\psi = \sqrt{k_\psi}$) and the structural damping coefficients ($d_\psi = 2\xi_\psi \omega_\psi$) can be computed from a given estimate of the damping ratio (ξ_ψ).

The structural equation is solved using the explicit fourth-order Runge-Kutta method.

C. Flow-structure coupling algorithm

At each time step, the structural motion and flow field are unknown and need to be solved iteratively coupling the fluid and structural systems in a fully coupled manner [6,23–25]. Since the grid is "glued" to the body surface and the shape of the body does not change with time and only yaws as a whole according to the dynamics of the (internal) torsion spring no interpolation is needed to track the surface nodes. Moreover, since only one grid is involved, it rotates with the

body and remains unchanged, while the free-stream condition is applied to the outer surface of the rotating grid.

The coupling procedure includes the following steps:

(a) The variables at new time level $n + 1$ of the flow and structural equations are initially set to be the known values at time level n. Using the flow field current solution, the aerodynamic forces and moments acting on the solid body are calculated.

(b) Using the aerodynamic forces and moments, the structural equation of motion is solved to determine the new yaw angle of the body.

(c) The grid is moved and the grid velocity (time metrics, the derivative of computational space in respect to computational time [20,25,26] at each node point is calculated according to the updated structural position.

(d) The flow field is calculated by solving the Navier-Stokes equations for the updated grid and structural position.

(e) Using the flow field solution, the aerodynamic forces and moments acting on the solid body are calculated.

(f) The maximum residuals for both solutions of the flow and the structural equation are checked. If the maximum residuals are greater than the prescribed convergence criteria, a subiteration procedure is initiated, step (b) is repeated and the next pseudotime level becomes $m + 1$ (keeping only the new time metrics for the $m + 1$ subiteration); otherwise, the flow field and the position of the body are done and the next new physical time step is started at step (b).

Since elasticity of the structure is represented only by the internal torsion spring, the rigid body can only rotate around the normal (Z) axis. Therefore, no interpolation is needed during the subiterations to find the location of the flow field boundary, as the grid for the flow field computations is attached to the body surface and rotates rigidly with it. If the convergence criteria are small enough the time accuracy of the schemes is kept.

D. Validation and verification

The computational fluid dynamics (CFD) code we use has been extensively tested over the years by the authors and others [4,21,26–37] for flows and configurations identical or similar to the one considered in the current paper. Other versions of the code were validated and verified in work by others for numerus cases of more complex configurations. The code was tested for the current configuration (i.e., a sharp slender body of revolution) for a wide range of flow conditions (subsonic as well as supersonic, laminar, and turbulent). Results had been checked against experimental data and found to be very satisfactory, e.g., Degani [36] and Degani and Schiff [31] tested this code against laminar flow data measured by Lamont [38] and showed an excellent agreement. Degani and Schiff [31] also checked the code against laminar flow surface oil flow visualization experiment [39] at Re = 26 000 and found good qualitative agreement. Degani and Levy [30] and Degani *et al.* [29] checked this code augmented with a turbulence model and a similar grid adjusted for an appropriate y^+ for conditions of the Lamont's turbulent flow experiments [38] and found an excellent agreement. Even in cases of relatively moderate grid resolutions; grid independency tests showed [33–35] that the main features of the flow (global forces and moments acting on the body, large scale vortical flow structure) were predicted correctly.

Experiments have shown that the flow around ogive-cylinder bodies at incidence is laminar even for Reynolds number (based on cylinder diameter) as high as $Re_D = 200\,000$. Lamont [38,40] classified the results of his extensive work into three flow regimes based on separation (laminar, transitional, and turbulent) where the laminar regime is almost independent of AOA in the range $20° \leqslant \alpha \leqslant 90°$. Lamont observed that for $Re_D = 400000$, the separation bubble is laminar and the reattachment might be turbulent. However, for $Re_D = 200000$, and below the separation bubble and the reattachment are all laminar. While primary separation for the laminar cases is located circumferentially approximately as early as $85°$ from the windward ray, for the fully turbulent cases its location is $110°$. Laminar computations [36] at $Re_D = 200000$ matches the surface pressure results

of Lamont including location of primary separation and reattachment. Separate computations [31] at $Re_D = 26000$ simulate an experiment [40] at $\alpha = 40°$ where surface oil flow photographs were taken. The primary separation lines are at about $90°$ $90°$ measured circumferentially from windward plane of symmetry, indicating laminar separation. The line of separations of the computed surface oil flow match those of the experiment photos. Zilliac *et al.* [41] did an experiment at $Re_D = 30000$ using a long ogive-cylinder body ($L/D = 16$). Using pressure transducer measurements and smoke visualization they showed that the flow separation was laminar and the line of separation was located circumferentially approximately $90°$ from the windward ray. Wardlaw and Yanta [12] did an experiment at $Re_D = 150000$ using slightly blunted tangent $3D$ ogive and $9.6D$ cylindrical afterbody ($L/D = 16$) at AOA of $45°$. They also reported that the separation was laminar. Dexter [42] conducted a set of experiments using three different forebodies at angles of attack between $\alpha = 25°$ and $\alpha = 90°$ and $Re_D = 100000$ and also reported that separations were laminar. Degani and Zilliac [11] with a similar body of $x/D = 16$ and for Reynolds numbers 17000, 26000, and 35000, found using a pressure transducer that the power spectra characteristics of the near wake are laminar even at AOA of $85°$. Lamont's results for fully turbulent separation were also computed with the above mentioned code [29,30] with the aid of a turbulence model identifying correctly the different characteristics of the turbulent primary separation, the turbulent separation bubble, and turbulent reattachment.

III. ANALYSIS OF THE FIXED BODY

All the computations presented here were carried out for the following flow parameters: free stream Mach number $M_\infty = 0.2$, Reynolds number, based on cylinder diameter, $Re_D = 30000$ and for angles of attack in the range $0° \leqslant \alpha \leqslant 65°$. As explained and justified above (Sec. II D) for these conditions the flow is laminar and therefore no turbulence model was used.

A. Influence of disturbance location

As mentioned earlier, at each AOA computations were carried out for at least three different disturbance locations and for each disturbance location, solutions were also obtained after disturbance removal. For four angles of attack ($30°$, $40°$, 500, and $60°$) additional disturbance locations were performed, as will be discussed later.

Figure 3 shows the side-force coefficient (Cy) time histories of four distinct angles of attack: $30°$, $40°$, $50°$ and $60°$. We note that the time histories throughout the paper incorporate the nondimensional time defined by $\tau = a_\infty t/D$. For each AOA a disturbance was placed near the tip; calculations of three disturbance' circumferential angles are presented: $4°$ (orange line), $94°$ (purple line), and $178°$ (green line) from the windward plane of symmetry. At AOA of $\alpha = 30°$ the flow of all three cases is almost steady, with very small asymmetry for disturbances at $4°$ and $178°$ ($Cy = 0.2$) and much larger for $94°$ ($Cy = -2.4$). At AOA of $\alpha = 40°$ the unsteadiness of the flow of all three cases is more pronounced, with large asymmetry for all three disturbances (mean side force $Cy = 1.7$, $Cy = -2.5$, $Cy = 3.2$, for disturbances at $4°$, $94°$, and $178°$, respectively). It is worth noting that while the case where the disturbance is near the windward plane is almost periodic the other two cases are nonstationary with small amplitudes relative to the mean Cy.

At AOA of $\alpha = 50°$ all three cases are nonstationary, with large mean Cy (2.1, -3.1, 1.6, for disturbances at $4°$, $94°$, and $178°$, respectively). Two of the cases show large amplitude, nonstationary oscillations while the third ($178°$ case) is almost steady. At $\alpha = 60°$ all three cases are nonstationary, with large amplitudes and mean Cy (1.4, -2.2, 1.4, for disturbances at $4°$, $94°$, and $178°$, respectively). It is noteworthy that in all AOA cases tested for this work, ranging from $20°$ to $65°$, the sign of the mean Cy of each disturbance was the same (i.e., negative for disturbance at $94°$). At $\alpha = 10°$ or below Cy was virtually zero.
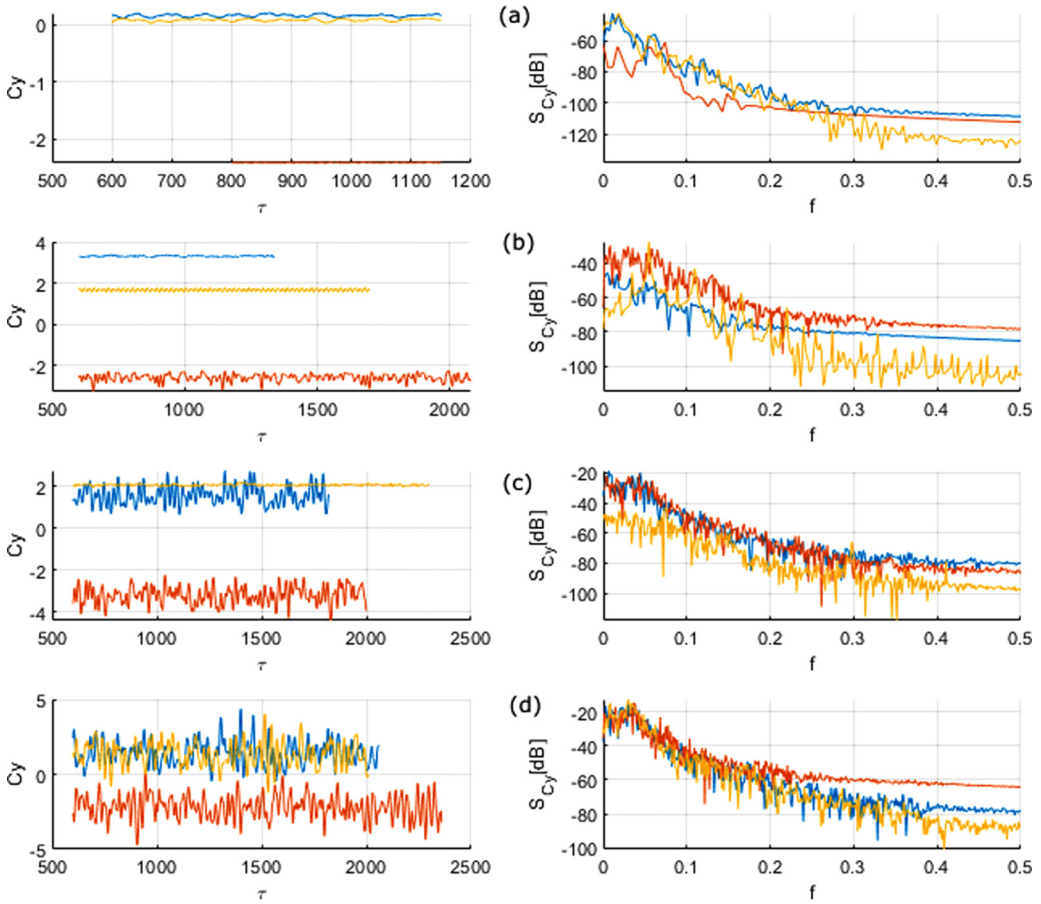
FIG. 3. Time histories and power spectra of side-force coefficient Cy of the flow around a fixed body at angles of attack $\alpha = 30°, 40°, 50°$, and $60°$, (a)–(d) respectively; and three disturbance locations: $4°$ (blue), $94°$ (red), and $178°$ (orange) circumferentially from the windward plane of symmetry.

B. Side force bifurcation structure

The bifurcation structure for a fixed body is investigated as a function of increasing AOA, both for cases where a disturbance was present and cases where the disturbance was used only as a trigger and was removed after initial time (of 300 nondimensional time units). Figure 4 depicts the time histories (left) and power spectra (right) of the side-force coefficient Cy cases where the initial disturbance was at $94°$ circumferentially from the windward plane of symmetry. Four representative angles of attack $\alpha = 30°, 40°, 50°$ and $60°$ are shown in Figs. 4(a), 4(b), 4(c), and 4(d), respectively. The flow is nonstationary as portrayed by the dense wide-banded power spectra. The change of the characteristics of Cy in comparison to the cases with the disturbances (see Fig. 3) is significant. For all four angles of attack the mean Cy is now zero or almost zero; the oscillations' amplitudes remain about the same at $\alpha = 60°$ but reduced drastically at $\alpha = 50°$ (and at $\alpha = 30°$ and $40°$ the amplitudes are negligible regardless of the disturbance existence).

As the time histories of the side-force coefficient Cy depicted in Figs. 3 and 4 are nonstationary, we portray in Fig. 5 both their average (a – Cy AVG)) and the root-mean square (b – Cy RMS) exerted by the flow on the body for cases where the body is held fixed for different angles of attack. For each AOA at least three cases of different disturbance locations were calculated. Since the solutions are nonstationary, every case was run long enough to obtain meaningful mean values of Cy
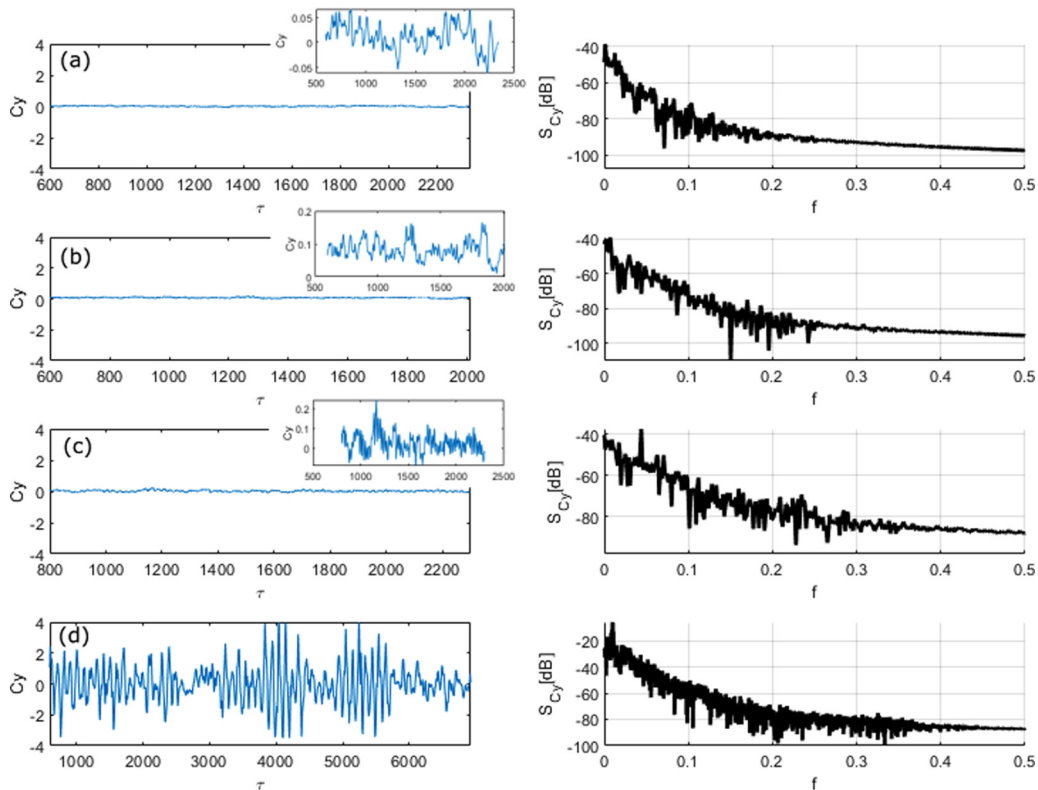
FIG. 4. Time histories (left) and power spectra (right) of side-force coefficient Cy for a fixed body after disturbance removal with angles of attack $\alpha = 30°$, $40°$, $50°$, and $60°$, (a)–(d) respectively.

and RMS of the oscillations' amplitudes (marked in Fig. 5 by orange triangles). For each AOA and disturbance locations computations were repeated where disturbances were used only as the initial trigger (marked in Fig. 5 by blue solid circles). Note that some of the symbols may be overlapped. As already demonstrated in Fig. 4, the disturbance removal reduces the mean Cy to zero or almost zero at all angles of attack.

For the cases without a disturbance [e.g., blue circles in Fig. 5(b)], one can divide the diagram into three regions: (A) steady (close to zero) solutions for $\alpha < 45°$, (B) transitional region in the range $45° < \alpha < 52°$, (C) nonstationary solutions region for $\alpha > 52°$. We note that the thresholds of the transitional region are determined primarily based on the possible formulation of a detached wake from the elliptic base ($\alpha = 45°$), while there is no shedding along the body, and the evolution of fully developed shedding along the body ($\alpha = 52°$) which interacts with the shedding from the base. These phenomena discussed in Sec. III C on the flow field analysis.

Furthermore, the removal of the disturbance represses the side-force amplitudes in regions A and B almost to zero. The same supercritical behavior for a fixed body at AOA below $52°$ was observed in previous computations for low angles of attack. It was shown [6] that for long body configurations when the disturbance was removed the flow relaxed to steadiness and the side force diminished completely. This difference between the behavior of long and short bodies may be explained by the existence of the unsteady wake at the end of the body (see Fig. 6).

The so-called bistable phenomenon:

From Fig. 5(a) it is evident that at $\alpha = 30°$, depending on disturbance's location, all values of mean Cy are possible. However, at higher AOA ($\alpha = 40°$ and above), a mean Cy lower than a certain
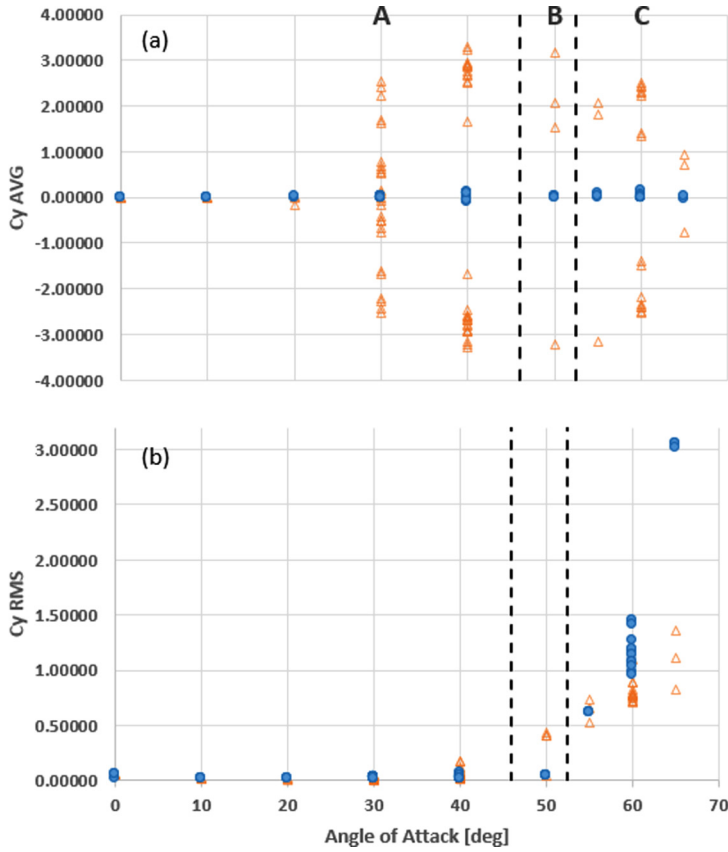
FIG. 5. Bifurcation diagrams for the averaged (a) and modulated RMS amplitude (b) side force coefficient as a function of AOA for a fixed body. Full circles (blue) – after disturbance removal, hollow triangles (orange) – with disturbance. We divided the diagram into three regions: A – steady solution, B – transitional and C - nonstationary.

value cannot be found. For example, at $\alpha = 40°$, no values in the range $-1.6 < Cy < 1.6$ can be found. It seems that the asymmetry has two preferred vortex positions (left hand or right hand). For this reason, some articles called this behavior bistable. Strictly speaking, this is not a bistability phenomenon, since after such a stable value is reached, if the disturbance is removed, the mean Cy would return to zero, or, if additional disturbance is added, the mean Cy (and the position of the vortices) will shift. This contradicts the requirement that the (stable) position should be stable to small disturbances (the basin's low potential energy). As a matter of fact, it was demonstrated experimentally [27] that by changing the disturbance incrementally, any value of mean Cy can be obtained between the bistable values. For all angles of attack tested (30° to 60°), no sign of hysteresis was observed, i.e., results obtained as the disturbance was first extended and then retracted were always virtually the same.

C. Flow field analysis

The effect of the unsteady wake at the end of the body is also evident from the flow visualization presented in Figs. 6 and 7. Figure 6 shows velocity magnitude contours at the vertical plane of symmetry for $\alpha = 30°$, 40°, 50° and 60° after disturbance removal. It is apparent that for $\alpha = 30°$, 40°, and 50° the wake has small effect on the flow over the body, that remains steady and symmetric. However, the velocity contours for $\alpha = 40°$ indicate to an attached blunt end wake whereas the wake
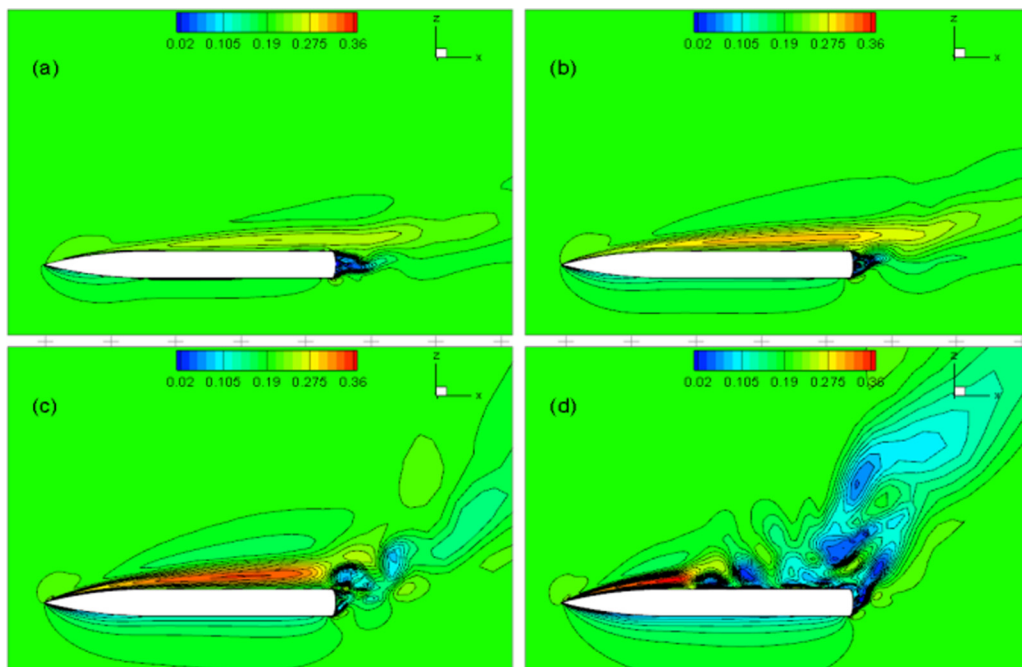
FIG. 6. Velocity magnitude contours of a fixed body after disturbance removal for (a) $\alpha = 30°$, (b) 40°, (c) 50° and (d) 60°.

for $\alpha = 50°$ appears detached similar to the appearance of detached wakes for fixed cylinders and spheres. In contrast to the two lower AOA cases, where the primary vortices are continuous from tip to the body's end and are almost parallel to the body's surface, at $\alpha = 60°$, the flow over the forehead is symmetric and steady but over the cylindrical part of the body is unsteady (and as will be shown next, vortex shedding also occurs) and the wake at the end of the body merges into it.

Figure 7 shows helicity density contours for $\alpha = 30°$, 40°, 50°, 60°. (Helicity density [43] is defined as the scalar product of the local velocity and vorticity vectors. Since it indicates both the strength and sense of rotation of the vortices, helicity density has been found to be an excellent means of visualizing the position and strength of the vortex pattern. By marking positive and negative values of helicity with different colors, it is easy to differentiate between the primary and secondary vortices.) For each AOA several cross sections along the body are shown and also (right side of Fig. 6) at $x/D = 5.2$, which is about mid-body location. At $\alpha = 30°$ and, 40°, all cross sections show perfect symmetry. At $\alpha = 50°$, the flow around the body is steady and symmetric but some asymmetry is evident near the end of the body due to the effect of the unsteady wake. At $\alpha = 60°$, the flow around the forehead is symmetric and steady but unsteady around the cylindrical afterbody.

The authors of Ref. [41] conjectured based on experimental measurements and flow visualizations that the flow around the pointed slender body at high AOA can be divided into three distinct regimes. If the cylinder part of the body is infinitely long, the first regime, which is the farther downstream of the nose, is far enough downstream that the nose influence on the flow there is negligibly small. Therefore, the flow in regime 1 is essentially the flow past an inclined cylinder; in the crossflow normal to the cylinder axis, the flow is essentially the 2D flow past a cylinder (parallel vortex shedding). Regime 3 (the nose, where the body grows from zero to the cylinder diameter) is steady (symmetric or asymmetric, depending on disturbance distribution/location). Regime 2 overlaps regimes 1 and 3 with time-dependent shedding of vortices as in regime 1 but the vortices
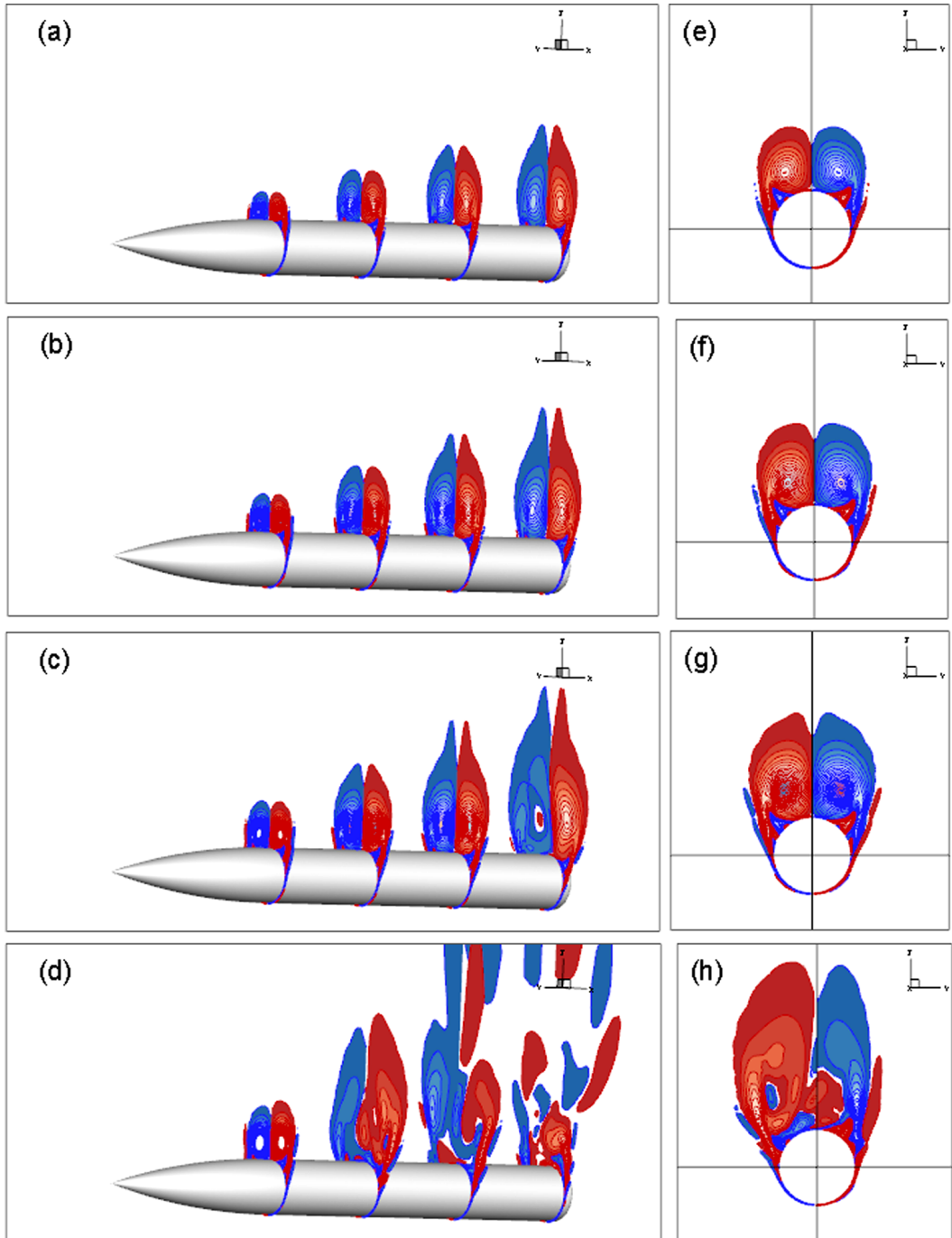
FIG. 7. Helicity density contours of a fixed body after disturbance removal for (a) $\alpha = 30°$, (b) 40°, (c) 50°, (d) 60° and helicity cross section at $x/D = 5.2$ for each angle (e)–(h), respectively.
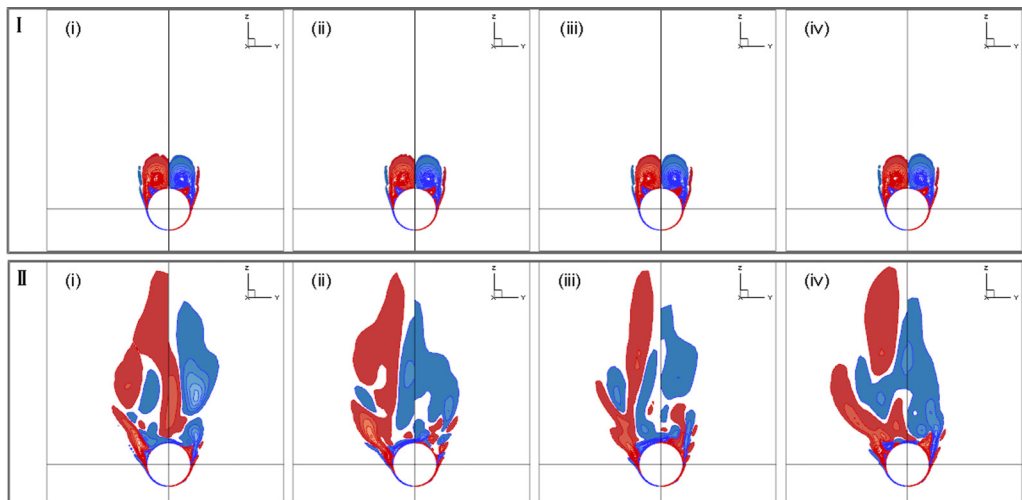
FIG. 8. Snapshots of helicity-density contours of a fixed body after disturbance removal for one period T = 100 [dimensionless time units] of major frequency (see Fig. 4) at axial location (I) $x/D = 3.0$ and, (II) 7.0 and AOA $\alpha = 60°$, with equal time interval of T/4, (i)–(iv), respectively.

are inclined obliquely to the cylinder axis. The authors of Ref. [41] found support to their conjecture in Ramberg's [44] experiments, which involved bodies of high fineness ratio ($L/D = 100$), where all three regimes are easily identifiable in the flow visualization. Since the body considered here is much shorter than the bodies in the above experiments ($L/D = 10$ in comparison to $L/D = 16$ of [41], $L/D = 100$), regime 1 is only evident here in the cases of AOA above 52° [regions B, C, Fig. 5, and visualization Figs. 7(d) and 7(g)]. The significant point is that even at high AOA, the flow regime around the nose, which includes the tip vortices, is steady [see Fig. 8(i) at $x/D = 3.0$, while highly unsteady along the cylindrical afterbody, see Fig. 8(ii) at $x/D = 7.0$].

In order to verify the extent of the body blunt-end effect on the flow upstream, we calculated the side-force coefficients on circular thin slices along the body of approximately 0.3D thick. Figure 9 shows the time histories of Cy of several of these slices. The values in the legend are the distance of the slice center from the tip of the body (which is 10D long). As can be seen, the oscillations decrease exponentially and are negligible at $x = 8.0D$ or less.

IV. ANALYSIS OF THE RESTRAINED BODY

A. Restrained yaw bifurcation structure

The slender body is constrained to yaw (ψ) within the x-y plane only and the spring attachment is located at the axis of rotation (which is also the origin of the coordinate system) defined at a distance of 5.2D downstream of the tip and on body centerline. The structural parameters, as defined in Eq. (3) are $k_\psi = 0.1$, $d_\psi = 0.0063$, $\mu = 5.6 \times 10^{-4}$. The corresponding natural frequency and damping ratio for these conditions are $\omega_\psi \sim 0.316$ (or $f_\psi \approx 0.05$) and $\xi_\psi = 0.01$, respectively. The flow conditions are identical to those of the fixed body (Sec. III A, above).

As was done for the fixed body, the computations started from a uniform flow field and time-accurate computations were carried out. To obtain solutions after disturbance removal, the computations were carried out with a disturbance for 300 nondimensional time units and then the disturbance was removed and computations continued. The motion of the solid body changes the flow significantly in comparison to the flow around the fixed body. Figures 10 and 11 show time histories (left) and power spectra (right) of the yaw angle, ψ, and side-force coefficients, Cy, for several angles of attack, after the disturbances are removed. At $\alpha = 10°$ and $\alpha = 30°$ [Figs. 10(a),
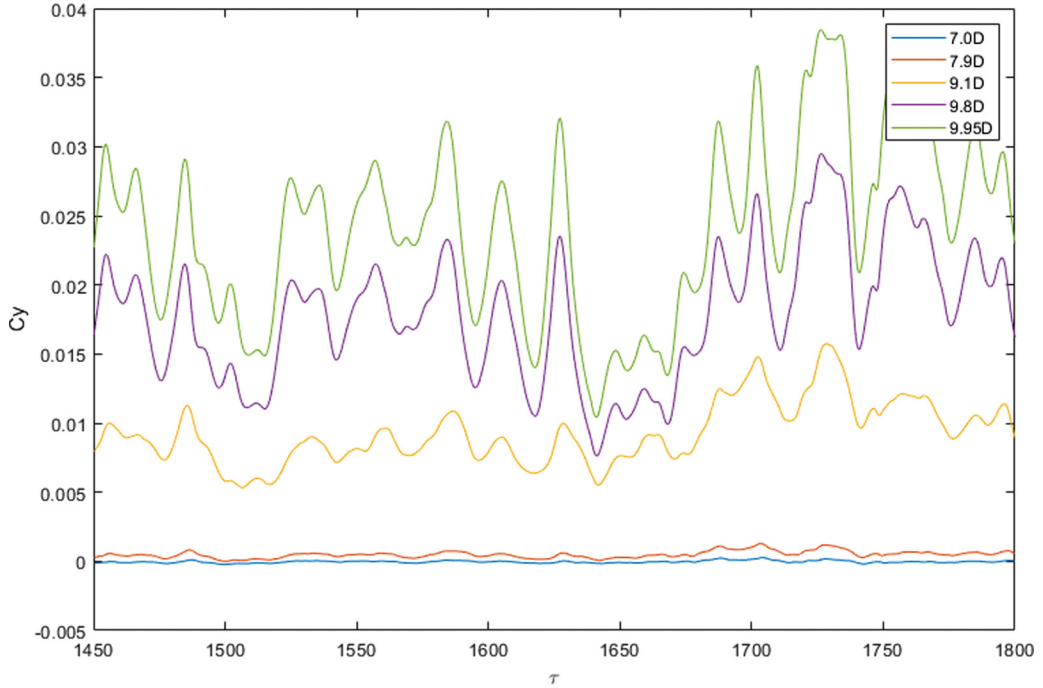
FIG. 9. Side-force coefficients of the flow around 0.3D thick slices along the body.

10(b), 11(a), and 11(b)] the side force Cy and angle ψ are almost harmonic, oscillating with a frequency of about 0.037. Note that although the peak of the side-force power spectra is identical to that of the yaw, there is a distinct phase shift between the corresponding time histories.

In order to classify the nonstationary solutions, we make use of a Poincare map sampled every upward zero cross section of the drag force time history [45]. Thus, periodic solutions incorporate a single point whereas nonstationary interactions culminate with a cloud of points as depicted in Fig. 12 where the Poincare maps defined by red circles are overlaid on the solution structural state space. We define the nonstationary Poincare maps as wide-spread transit or localized nontransit if their Poincare points completely cover the state space [Figs. 12(e) and 12(f)] or are localized to a specific area of the state space [Fig. 12(c) and 12(d)] for large or intermediate angles of attack, respectively. We note that transit and nontransit nonstationary solutions were documented for the chaotic dynamics of a pretensioned string [46,47] and more recently for the nonstationary vortex-induced vibration of a tethered sphere [48].

In addition to the finite amplitude periodic solution there is a coexisting small amplitude solution at AOA $\alpha = 30°$, which is not periodic [Figs. 10(c) and 11(c)]. At $\alpha = 40°$ the yaw is almost periodic [Figs. 10(d) and 11(d)] while at $\alpha = 50°$ and $\alpha = 60°$ is nonstationary [Figs. 10(e), 10(f), 11(e), and 11(f), respectively].

Figure 12 depicts the state space and overlaid Poincare map, defined by sampling the moment every positive zero crossing, at $\alpha = 30°, 40°, 45°, 55°, 60°, 65°$, (a)–(f), respectively. All cases here have a large amplitude yaw angle magnitude, where cases (a) and (b) show periodic behavior (regions II and III, Fig. 14), all the rest are nonstationary, while (c) and (d) are nontransit and (e) and (f) are transit nonstationary cases.

Figure 13 presents the state space and overlaid Poincare map (red circles), and the correspondent power spectra, for $\alpha = 24°, 26°, 30°$, and $34°$ of the lower branch of the region II in the bifurcation diagram [Figs. 14(a)–14(d), respectively]. The lower branch begins with a nonstationary ($24°$) and ends with a nontransit quasiperiodic solution ($34°$).
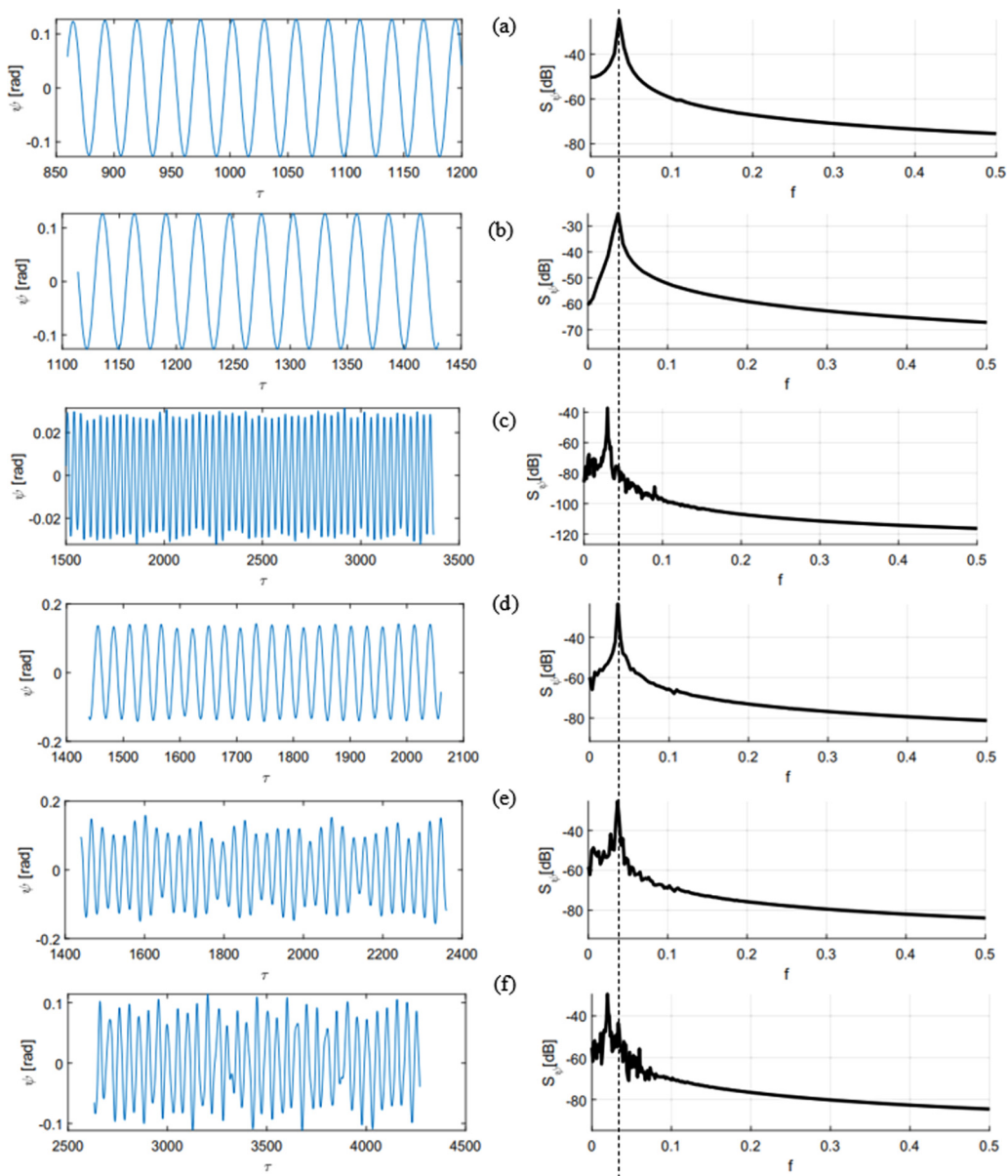
FIG. 10. Time histories (left) and power spectra (right) of yaw angle (ψ) of a restrained body after disturbance removal for (a) $\alpha = 10°$, (b) $30°$ (high), (c) $30°$ (low), (d) $40°$, (e) $50°$, (f) $60°$. Spring stiffness $k_\psi = 0.1$. Note that cases (a), (b), and (d) are periodic, case (c) has low yaw angle amplitude, (e),(f) exhibit nonstationary behavior. The dashed line shows the frequency ~ 0.037, which is the same for all high amplitude cases for regions I–IV.

The behavior of the restrained yaw angle (ψ) amplitude after disturbance removal can be summarized in a bifurcation diagram (Fig. 14) for the range of angles of attack up to $65°$. As explained earlier, for each AOA three different disturbance locations were calculated; at circumferential angle $\Phi \sim 2°$ off the leeward plane of symmetry, at $\Phi = 90°$, i.e., perpendicular to windward plane of symmetry and at $\Phi \sim 176°$. For each case, the disturbance was removed after 300 nondimensional
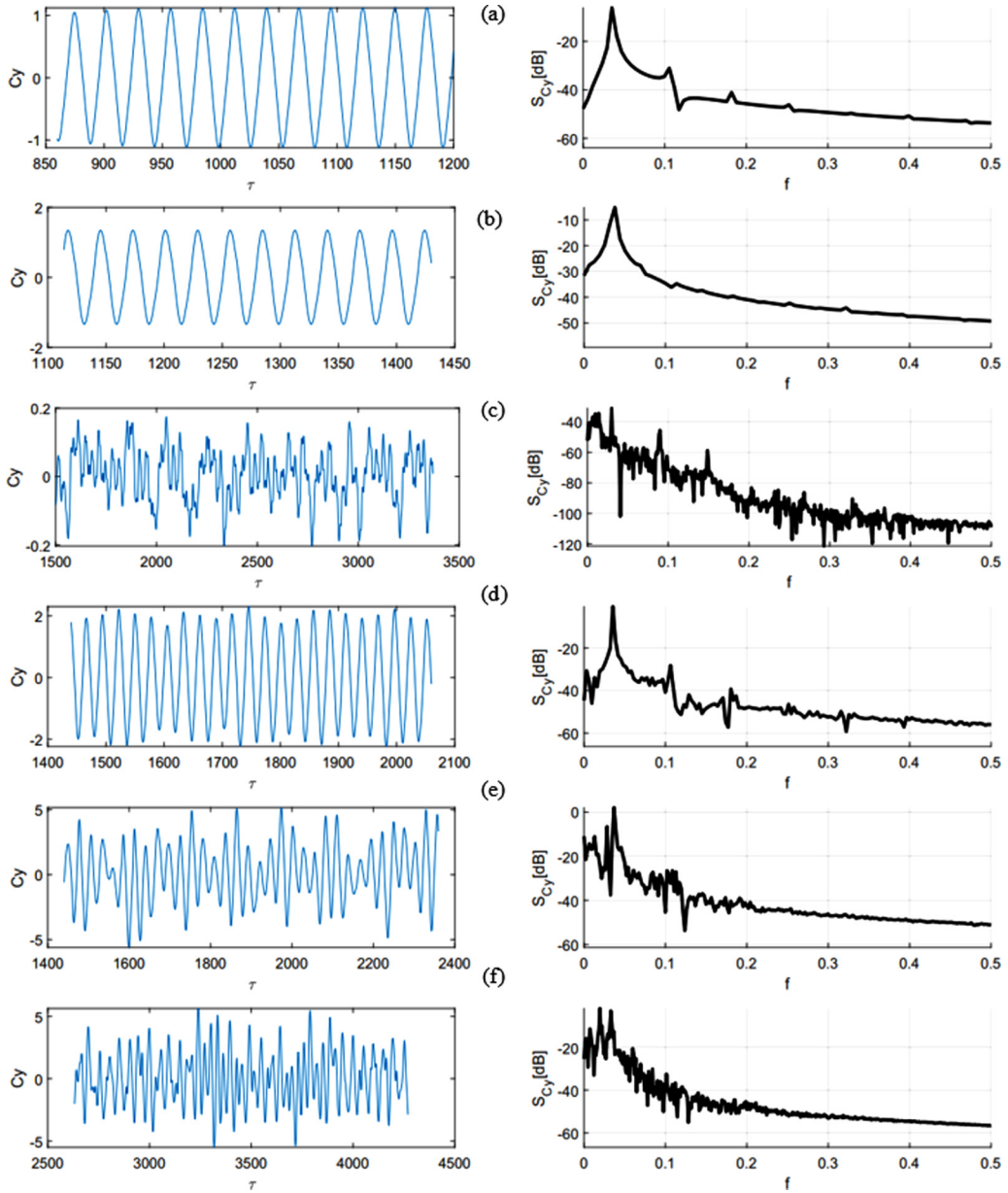
FIG. 11. Time histories (left) and power spectra (right) of side-force coefficient Cy for a restrained body after disturbance removal for (a) $\alpha = 10°$, (b) $30°$ (high), (c) $30°$ (low), (d) $40°$, (e) $50°$, (f) $60°$. Spring stiffness $k_\psi = 0.1$.

time units and calculations continued. Therefore, in the diagram three cases are depicted for each AOA but for $\alpha < 40°$, at each angle they converged to the same solution. The bifurcation structure can be divided into five regions: (I) finite amplitude periodic oscillations at low angles of attack, (II) bistable finite amplitude periodic coexisting with small amplitude aperiodic oscillations, (III) finite amplitude periodic oscillations at moderate angles of attack, (IV) nonstationary transit oscillations, (V) nonstationary nontransit oscillations. Figure 15 depicts an identical bifurcation diagram for the
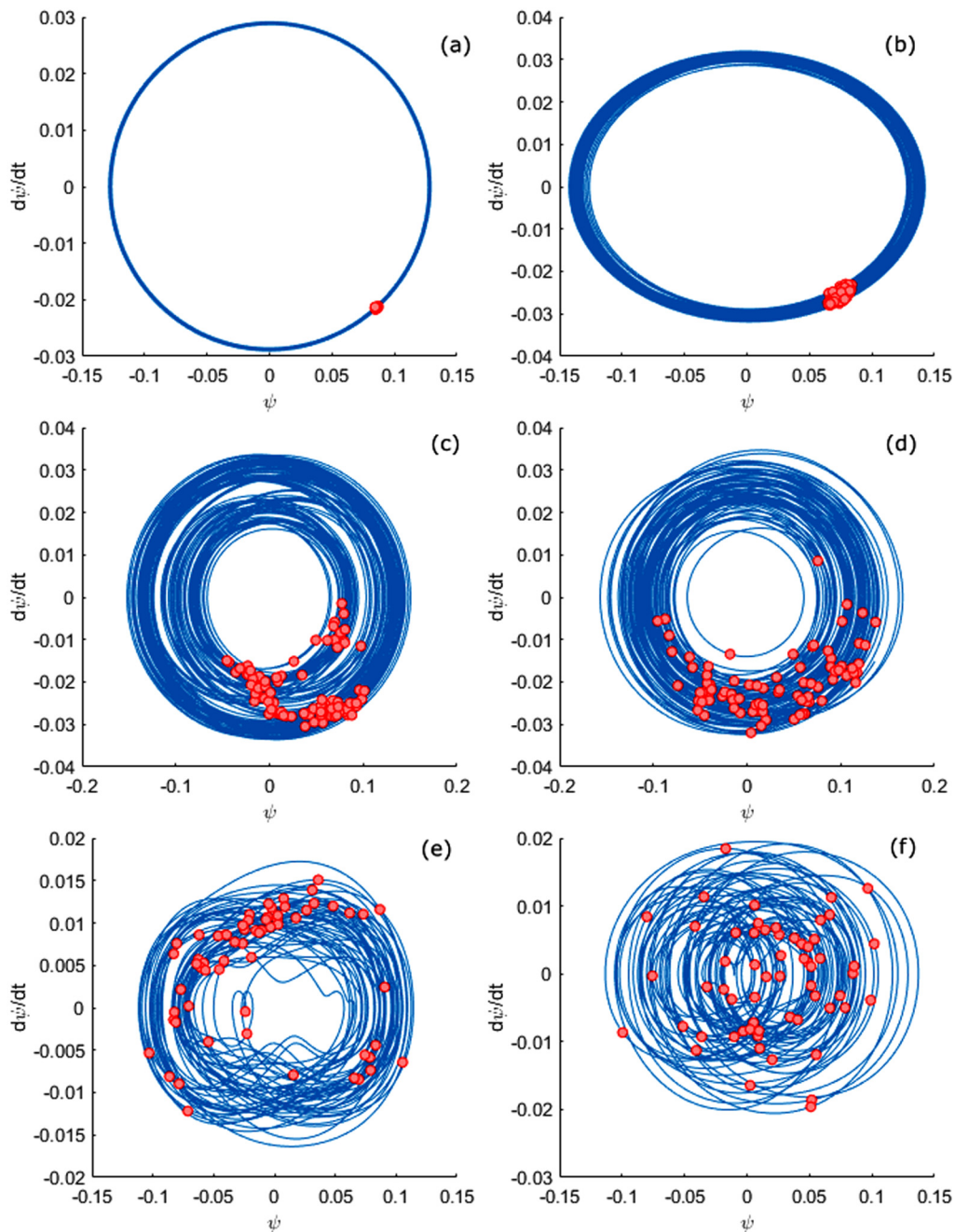
FIG. 12. State-space diagrams and overlaid Poincare maps (red circles), defined by sampling the moment every positive zero-crossing, at (a) $\alpha = 30°$, (b) $40°$, (c) $45°$, (d) $55°$, (e) $60°$, (f) $65°$. Spring stiffness $k_\psi = 0.1$. All cases here have a large amplitude yaw angle magnitude, where cases (a) and (b) show periodic behavior (regions II and III, Fig. 14), all the rest are nonstationary. Note that (c) and (d) are localized nontransit whereas (e),(f) are wide-spread transit Poincare maps.
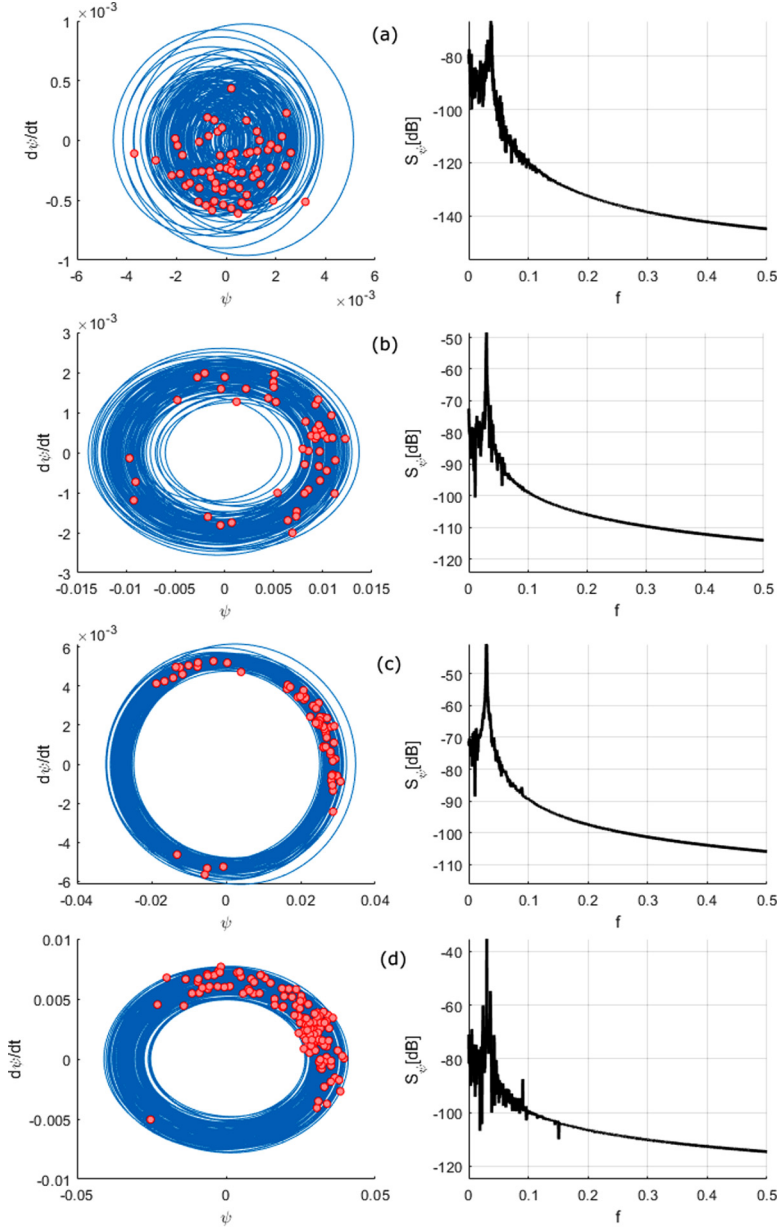
FIG. 13. State-space diagrams and overlaid Poincare maps (red circles), for (a) $\alpha = 24°$, (b) 26°, (c) 30° and (d) 34° of the lower branch of the region II of the bifurcation diagram (Fig. 14). The lower branch starting as nonstationary ($\alpha = 24°$) and ends with periodic like solution ($\alpha = 34°$). Spring stiffness $k_\psi = 0.1$.

side-force coefficients acting on the body as a function of AOA, where the Cy amplitudes in regions IV and V are significantly higher than those in regions I, II, and III.

A comparison of the side force between the fixed and the restrained configurations after disturbance removal reveals a significant increase of side-force oscillation amplitude for the latter. We note that the nonstationary region for the fixed case (see Fig. 5, region C) corresponds to that of
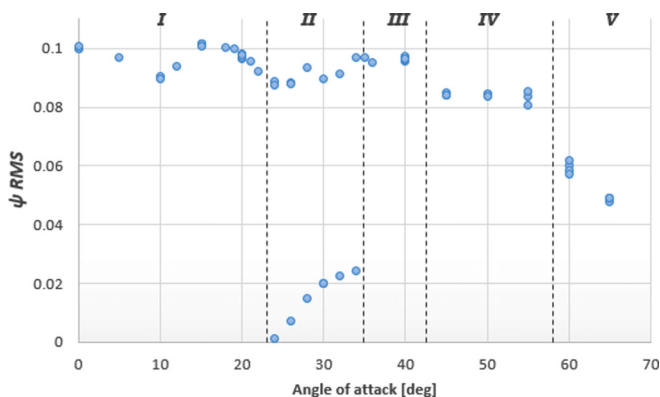
FIG. 14. Bifurcation diagram of the yaw angle amplitude of a restrained body after disturbance removal. Spring stiffness $k_\psi = 0.1$. The diagram divided to five regions: (I) large amplitude periodic oscillations at low angles of attack, (II) bistable/coexisting large and small amplitudes, (III) large amplitude periodic oscillations at moderate angles of attack, (IV) nonstationary transit oscillations, (V) nonstationary nontransit oscillations.

the restrained case (see Fig. 15, regions IV and V) for high angles of attack ($\alpha > 42°$). However, for low and moderate angles of attack the side force of the restrained case is an order of magnitude higher (see Fig. 15) than that of the fixed case (see Fig. 5). Furthermore, the restrained configuration
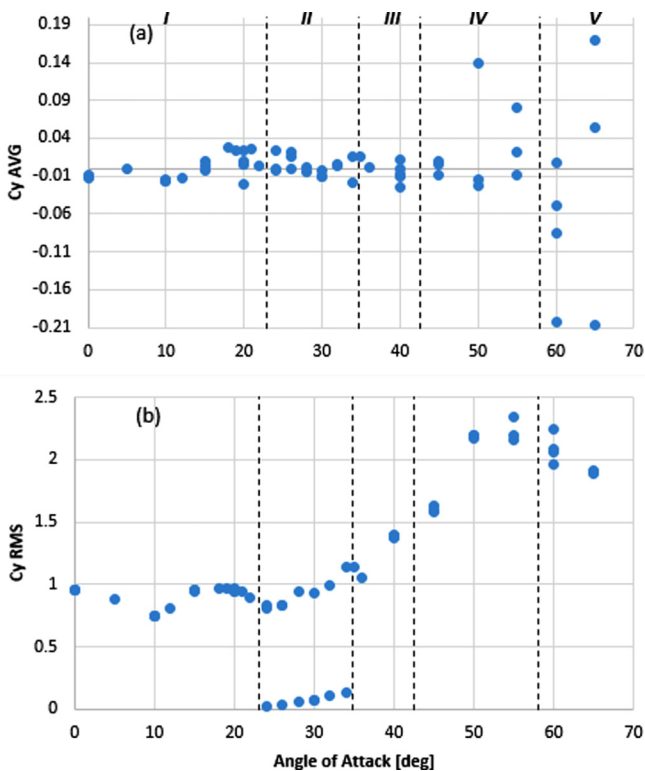

FIG. 15. Bifurcation diagrams for the averaged (a) and modulated RMS amplitude (b) side force coefficient as a function of AOA for a yaw restrained body after disturbance removal. Spring stiffness $k_\psi = 0.1$.
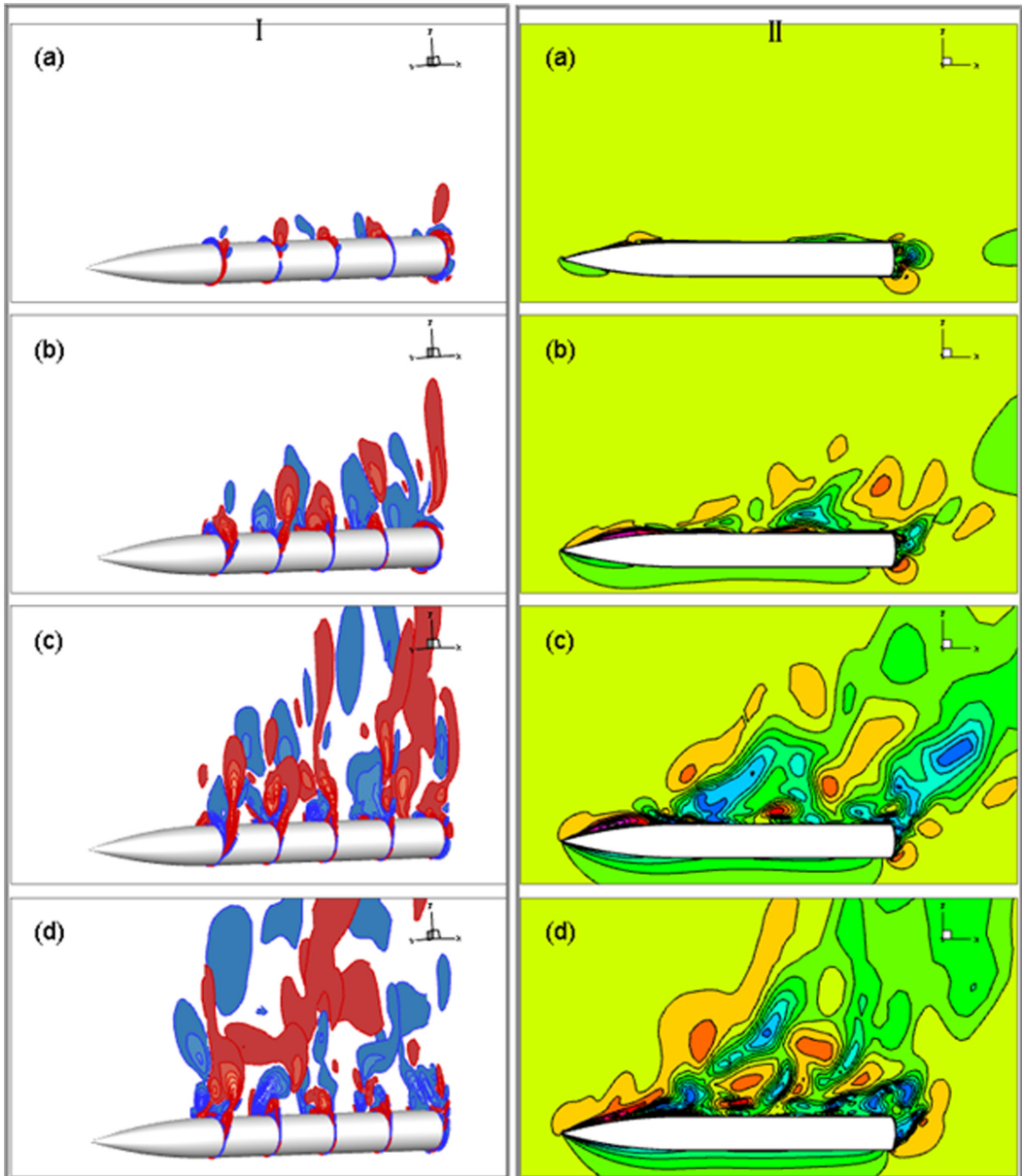
FIG. 16. Helicity density and velocity magnitude contours (I and II, respectively) of a restrained yaw body after disturbance removal for (a) $\alpha = 10°$, (b) 30°, (c) 50°, (d) 60°.

introduces bistable solutions that do not exist for the fixed case for moderate angles of attack (22° $< \alpha < 35°$).

B. Flow field analysis

The differences shown in the previous section are also evident from the flow visualization presented in Figs. 16, 17, and 18. Figure 16(I) shows helicity density at several cross sections along the body for $\alpha = 10°$, 30°, 40°, 50°, 60° and Fig. 16(II) shows velocity magnitude contours
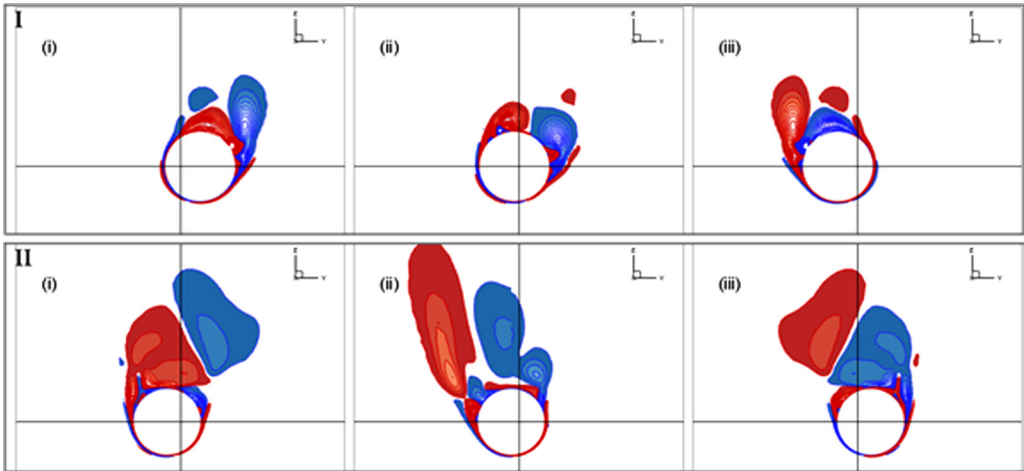
FIG. 17. Snapshots of helicity density contours for one period at axial locations $x/D = 3.0$ and 7.0 (I and II, respectively) at AOA $\alpha = 30°$.

at the vertical plane of symmetry for the same angles of attack. They demonstrate the different charcteristics of each AOA but also demonstrate the difference between the cases of the fixed body (Figs. 4 and 5) and the yaw-restrained body cases. Even at the low and intermediate AOA cases of $\alpha = 10°$ and $30°$ the primary vortices along the cylindrical afterbody are no longer uniform and they break to small segments. At the higher AOA ($\alpha = 50°$ and $60°$) the flow is nonstationary. To emphasize the latter, Figs. 17 and 18 show the series of helicity density snapshots of one time period T at two locations along the body ($x/D = 3.0$ and $x/D = 7.0$). At $\alpha = 30°$, where the motion of the body is periodic, the vortices along the front part of the body just change orientation from left hand to right hand and vice versa following the periodic motion of the body [Fig. 17(I), $x/D = 3.0$, Fig. 17(II), $x/D = 7.0$]. However, at $60°$ the wake along the cylindrical afterbody is irregular [Fig. 18(II), $x/D = 7.0$] and even at the nose, where the flow was symmetric and steady for the
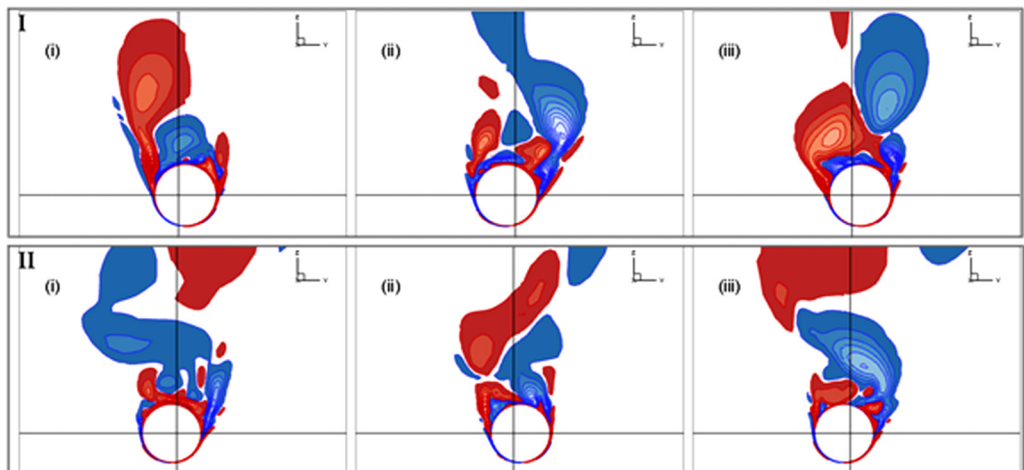

FIG. 18. Snapshots of helicity density contours for one period at axial locations $x/D = 3.0$ and 7.0 (I and II, respectively) at AOA $\alpha = 60°$.
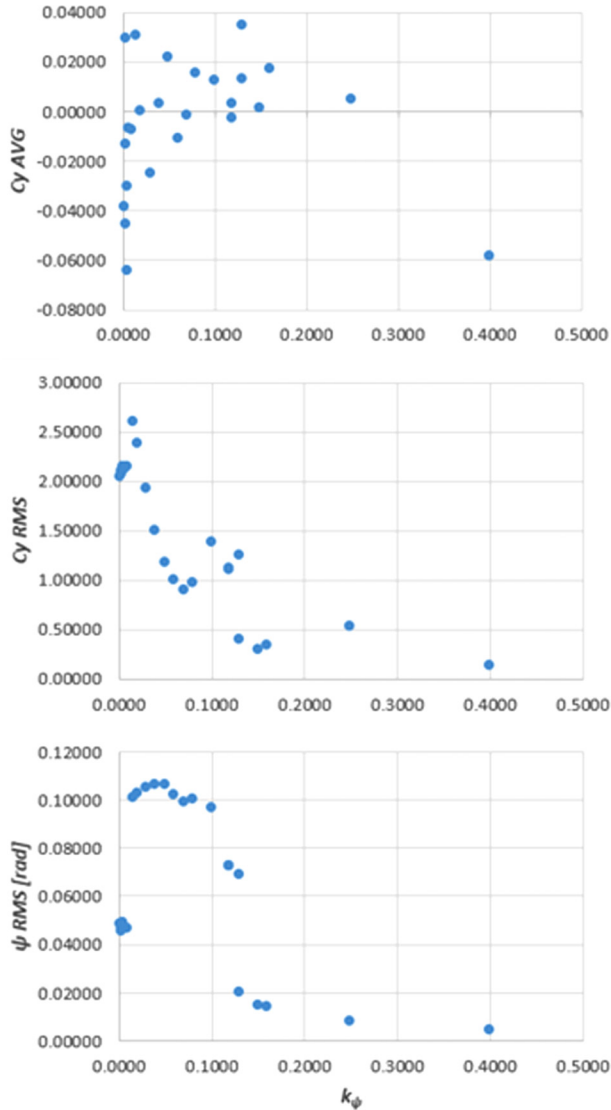
FIG. 19. Bifurcation diagrams for the yaw angle amplitude vs torsion spring stiffness coefficient, for AOA $\alpha = 40°$, starting with a soft spring ($k_\psi = 0.002$) to a hard spring ($k_\psi = 0.4$). Maximum yaw amplitude is obtained for a spring with $k_\psi = 0.04$.

fixed body, vortices are shed in a nonstationary manner while orientation changes from left hand and right hand and vice versa following the yaw motion of the body [Fig. 18(I), $x/D = 3.0$].

C. Influence of the torsion spring stiffness

In Fig. 19 we summarize the effect of the torsion spring stiffness on yaw amplitude and side-force coefficients, beginning with a soft spring ($k_\psi = 0.002$) and ending with a stiff spring ($k_\psi = 0.4$). We select an AOA $\alpha = 40°$ for the analysis as it is representative of region III, which has a unique periodic limit cycle. The maximum yaw amplitude is obtained for a spring with $k_\psi = 0.04$ whereas the maximum amplitude of the modulated side force (Cy Amp in Fig. 19) occurs for a slightly lower

k_ψ.. As expected, the lowest yaw amplitude was obtained for the stiffest spring. On the other hand, for values below $k_\psi = 0.04$ the amplitudes of the yaw drop but the side-force amplitudes do not. We note that the characteristic of the yaw amplitude time history changes as the stiffness is varied. Low values of stiffness $k_\psi < 0.04$ exhibit nonstationary response whereas stiffness values in the range $0.04 < k_\psi < 0.015$ yield of periodic or quasiperiodic solutions. Higher values of stiffness where $k_\psi > 0.015$ consist of nonstationary solutions with diminishing amplitudes for both yaw and side-force amplitudes.

As can be seen from Fig. 19, for spring stiffness up to $k_\psi = 0.1$ or so, the amplitudes of Cy are comparable with those obtained for the fixed body of $\alpha = 60°$ and $65°$. In these fixed body cases, the Cy time histories were nonstationary. The Cy time histories for the restrained yaw configuration change between nonstationary to periodic or quasiperiodic. However, for the very stiff spring of $k_\psi = 1$ (not shown), Cy amplitude reduces to 0.1 with a wide banded power spectrum similar to the case of the fixed body, for $\alpha = 40°$. It is worth mentioning that the average of Cy is very small but not zero.

The bifurcation diagram in Fig. 19 can be reposed as the dependence of the yaw limit-cycle amplitude as a function of the reduced velocity (U^*):

$$U^* = \left(\frac{U_\infty}{D f_\psi} \right) = \left(\frac{2\pi M_\infty}{\sqrt{k_\psi}} \right), \tag{4}$$

where U_∞ is the free stream velocity, D is the body diameter, f_ψ is the system natural frequency, M_∞ is the free stream Mach number, and k_ψ is the normalized torsion stiffness.

Figure 20 shows the maximum yaw limit-cycle amplitude (a), and its corresponding limit-cycle frequency (b) normalized by the system natural frequency as a function of the reduced velocity, for three angles of attack, $\alpha = 20°$, $30°$, and $40°$. We identify a classical bifurcation structure where for the case of $\alpha = 40°$ (blue dots in Fig. 20) lock-in occurs in the range $4 < U^* < 10$ and desynchronized solutions occur in the range $0 < U^* < 4$ and in the range $U^* > 10$. The lock-in range is characterized when the ratio between the limit cycle and natural frequency is close to unity [Fig. 20(b)]. For the cases of $\alpha = 30°$ (grey dots in Fig. 20) and of $\alpha = 20°$ (orange dots in Fig. 20) the lock-in range the width of the lock-in range reduces significantly and solution in the desynchronized region with a large reduced velocity increase in magnitude culminating with large amplitude oscillations (e.g., $\psi_{RMS} = 0.255$ for $U^* = 15$ corresponding to a weak torsion spring stiffness of $k_\psi = 0.007$).

We recall that while the desynchronized region in both circular [49] and elliptical cylinders [50] has been shown to have small transverse limit-cycle amplitudes, the desynchronized region for a tethered sphere has been shown to increase in magnitude of transverse amplitudes [51–53].

Figure 21 depict the state space and overlaid Poincare map, for $\alpha = 30°$ with $k_\psi(U^*) = 0.07(4.7)$, $0.007(15.0)$, We note that the response is periodic for the maximal value of the yaw amplitude within the lock-in region ($U^* = 4.7$) whereas the desynchronized response ($U^* = 15.0$) consists of a transit nonstationary solution which is portrayed by an irregular Poincare map and a wide banded power spectra [Fig. 21(b)].

Figure 22 depicts the state space and overlaid Poincare map, for $\alpha = 40°$ with $k_\psi(U^*) = 0.04(6.28)$, and $0.005(17.8)$. We note that the response is a nontransit quasiperiodic solution for the maximal value of the yaw amplitude within the lock-in region ($U^* = 6.28$) whereas the desynchronized response ($U^* = 17.8$) consists of a transit nonstationary solution, which is portrayed by an irregular Poincare map and a wide banded power spectra [Fig. 22(b)].

We summarize the influence of the torsional spring stiffness for the considered angles of attack with a similar resonant lock-in bifurcation structure. We observed a striking difference between the periodic synchronized lock-in for $\alpha = 20°$ and $30°$ and the nontransit quasiperiodic lock-in for $\alpha = 40°$ and note that the former is similar to that of restrained circular cylinders and tethered spheres in uniform laminar flow or significantly lower Reynolds numbers.
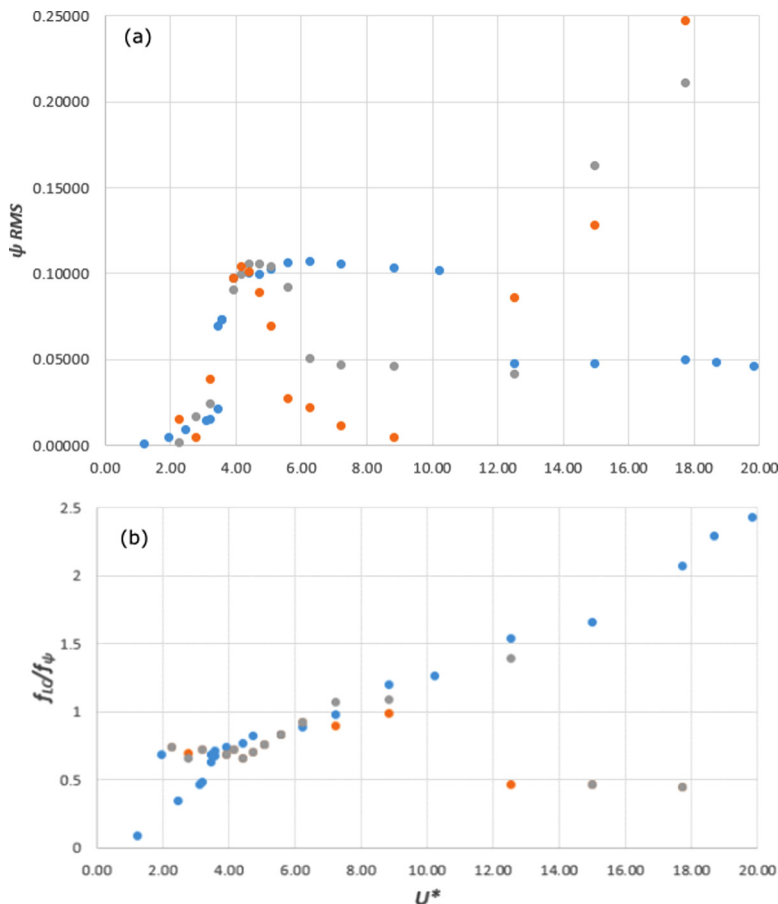
FIG. 20. Bifurcation diagrams for the maximum yaw angle amplitude (a), and (b) normalized limit cycle oscillation frequency as a function of a normalized reduced velocity (U^*), for $\alpha = 40°$, $30°$, $20°$ (blue, gray, and orange circles).

V. CLOSING REMARKS

We conducted a numerical investigation of the flow around an inclined tangent ogive-cylindrical body of a finite length, placed in a wind tunnel at a high AOA and allowed to yaw in x-y plane. The body is subjected to three-dimensional, compressible, laminar flow at a Reynolds number of 30 000 based on the body diameter and a Mach number of 0.2. A second-order accurate implicit finite difference scheme is employed for the flow equations, adapted to three-dimensional curvilinear coordinate system, whereas the coupled structural equation is solved by an explicit fourth-order Runge-Kutta method. We describe the investigation of the fluid-structure interaction in the range of $0° \leqslant \alpha \leqslant 65°$, both for fixed and restrained-yaw configurations.

The flow around the fixed body after disturbance removal for $\alpha > 52°$, is nonstationary with finite amplitude oscillations; whereas in the range $0° < \alpha < 52°$ the flow is almost steady with small nonstationary amplitude oscillations due to the body's blunt end nonstationary wake. We note that for $\alpha < 45°$ the body end wake is attached and we determined a transition region $45° < \alpha < 52°$ where the wake becomes detached similar to the onset of vortex induced vibrations in restrained cylinders and tethered spheres.
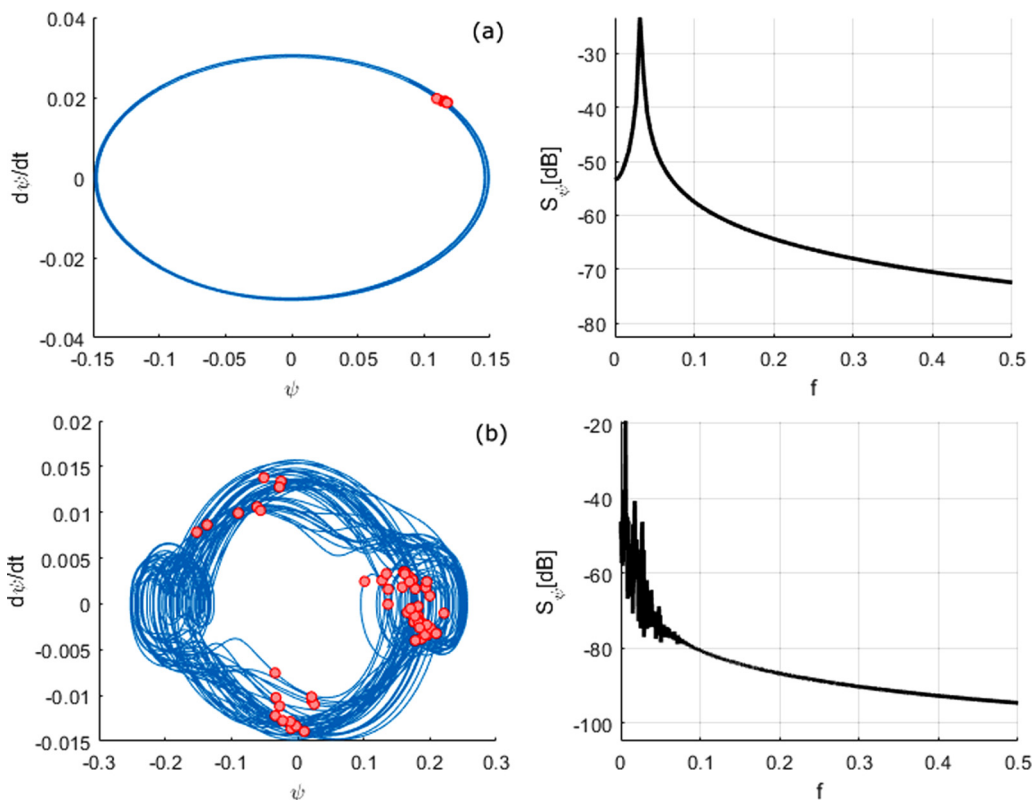
FIG. 21. State-space diagrams and overlaid Poincare maps (red circles - left) with corresponding power spectra (right) for $\alpha = 30°$ with (a) $k_\psi (U^*) = 0.07(4.7)$, and, (b), $k_\psi (U^*) = 0.007(15.0)$.

The resulting yaw response for a selected dimensionless torsional stiffness of $k_\psi = 0.1$ exhibits an intricate bifurcation structure for low and moderate angles of attack ($0° < \alpha < 42°$). We identify a bistable region ($22° < \alpha < 35°$) with periodic finite amplitude, which coexists with nonstationary low amplitude solutions, respectively. Furthermore, our analysis of the nonstationary solutions reveals a transition from nontransit quasiperiodic-like solutions ($42° < \alpha < 57°$) to transit chaoticlike solutions ($\alpha > 57°$) where the Poincare map points completely cover the yaw state space.

The physical significance of the bifurcation structure is that the fluid-structure interaction is dominated by the structural response which exhibits dominant regularization in the form of periodic finite RMS amplitude side-force values ($1 < CyRMS < 2$) for small and moderate angles of attack which for a fixed configuration were significantly smaller and nonstationary. Furthermore, the response to large angles of attack were nonstationary (quasiperiodic or chaoticlike) with comparable side-force amplitudes to those of the fixed configuration. However, the power spectra of Cy, while wide banded was distinctly different than the spectra of the fixed configuration demonstrating the dominance of the structural natural frequency into the fluid-structure interaction.

Investigation of the restraint torsion stiffness parameter reveals a resonant periodic lock-in phenomena for low angles of attack ($\alpha = 20°, 30°$), which becomes quasiperiodic for a moderate AOA ($\alpha = 40°$).

The possible occurrence of the above nonlinear fluid-structure interaction phenomena should be taken into account when such a body is mounted on an elastic sting in wind tunnel experiments, particularly when a force balance is used.
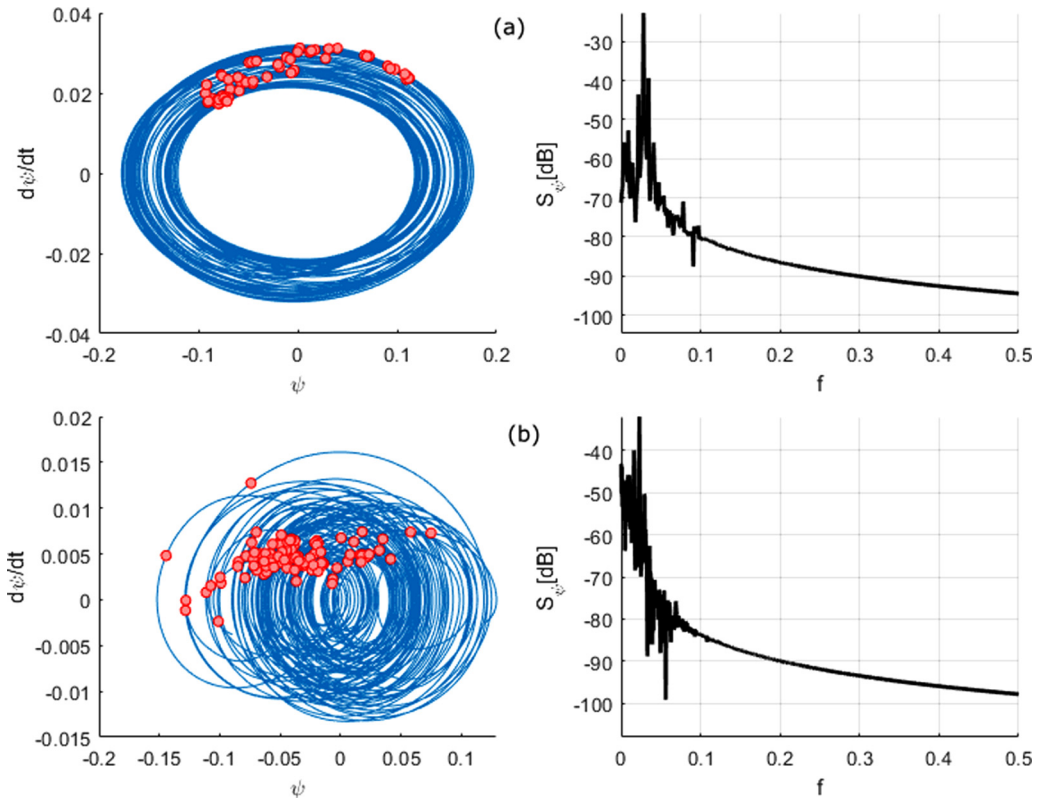
FIG. 22. State-space diagrams and overlaid Poincare maps (red circles) and corresponding power spectra for $\alpha = 40°$ with (a) $k_\psi(U^*) = 0.04(6.28)$ and (b) $k_\psi(U^*) = 0.005(17.8)$.

ACKNOWLEDGMENTS

[1] P. J. Lamont and B. L. Hunt, Pressure and force distributions on a sharp-nosed circular cylinder at large angles of inclination to a uniform subsonic stream, J. Fluid Mech. **76**, 519 (1976).

[2] D. Degani and M. Tobak, Effect of upstream disturbance on flow asymmetry, in *AIAA Aerospace Sciences Meeting* (AIAA, Reston, VA, 1992), Paper-92-0408.

[3] O. Wysocki and E. Schülein, Experimental investigations on the phantom yaw effect on a maneuvering slender body, J. Spacecr. Rockets **52**, 264 (2015).

[4] S. Gendel, O. Gottlieb, and D. Degani, Fluid-structure interaction of an elastically mounted slender body at high incidence, AIAA J. **53**, 1309 (2015).

[5] A. Kleiman, S. Gendel, D. Degani, and O. Gottlieb, Self-excited dynamics of an elastically restrained slender rigid body in uniform compressible laminar flow, Nonlinear Dyn. **86**, 2207 (2016).

[6] D. Degani, M. Ishay, and O. Gottlieb, Fluid-structure interaction of a rolling restrained body of revolution at high angles of attack, Phys. Fluids **29**, 037106 (2017).

[7] B. F. Ma and T. X. Liu, Low-frequency vortex oscillation around slender bodies at high angles-of-attack, Phys. Fluids **26**, 091701 (2014).

[8] O. Obeid, I. AlQadi, and J. AlMutairi, Investigation of asymmetric flow past a slender body at high angles of attack, Theor. Comput. Fluid Dyn. **33**, 481 (2019).

[9] T. L. Morse, R. N. Govardhan, and C. H. K. Williamson, The effect of end conditions on the vortex-induced vibration of cylinders, J. Fluids Struct. **24**, 1227 (2008).

[10] J. Zhao, K. Hourigan, and M. C. Thompson, Flow-induced vibration of d-section cylinders: An afterbody is not essential for vortex-induced vibration, J. Fluid Mech. **851**, 317 (2018).

[11] D. Degani and G. G. Zilliac, Experimental study of nonsteady asymmetric flow around an ogive-cylinder at incidence, AIAA J. **28**, 642 (1990).

[12] A. B. Wardlaw and W. J. Yanta, Asymmetric flow field development on a slender body at high incidence, AIAA J. **22**, 242 (1984).

[13] J. Cai, F. Liu, and S. Luo, Stability of symmetric vortices in two dimensions and over three-dimensional slender conical bodies, J. Fluid Mech. **480**, 65 (2003).

[14] J. Cai, H. M. Tsai, S. Luo, and F. Liu, Stability of vortex pairs over slender conical bodies: Analysis and numerical computation, AIAA J. **46**, 712 (2008).

[15] G. Easanesan, D. Burton, and M. C. Thompson, The effects of nose-shape and upstream flow separation on the wake of a cylindrical square-backed body, Exp. Therm. Fluid Sci. **118**, 110142 (2020).

[16] T. H. Pulliam and J. L. Steger, Implicit finite-difference simulations of three-dimensional compressible flow, AIAA J. **18**, 159 (1980).

[17] R. M. Beam and R. F. Warming, An implicit factored scheme for the compressible Navier-Stokes equations, AIAA J. **16**, 393 (1978).

[18] H. Lomax, T. H. Pulliam, and D. W. Zingg, *Fundamentals of Computational Fluid Dynamics* (Springer, Berlin, 2001).

[19] T. H. Pulliam and D. W. Zingg, *Fundamental Algorithms in Computational Fluid Dynamics* (Springer, Berlin, 2014).

[20] J. L. Steger, Implicit finite-difference simulation of flow about arbitrary two-dimensional geometries, AIAA J. **16**, 679 (1978).

[21] D. Degani and S. W. Marcus, Thin vs full Navier-Stokes computation for high-angle-of-attack aerodynamics, AIAA J. **35**, 565 (1997).

[22] L. Meirovitch, *Methods of Analytical Dynamics* (Wiley, New York, 1988).

[23] X. Y. Chen and G. C. Zha, Fully coupled fluid-structural interactions using an efficient high resolution upwind scheme, J. Fluids Struct. **20**, 1105 (2005).

[24] E. L. Blades and J. C. Newman, Aeroelastic effects of spinning missiles, in *Collection of Technical Papers - AIAA/ASME/ASCE/AHS/ASC Structures, Structural Dynamics and Materials Conference* (AIAA, Reston, VA, 2007), Paper-07-2243.

[25] J. R. Cebral and R. Löhner, Conservative load projection and tracking for fluid-structure problems, AIAA J. **35**, 687 (1997).

[26] S. Gendel, Nonlinear spatio-temporal flow-structure interaction of an elastically attached slender body at high incidence, Ph.D. dissertation, Technion–Israel Institute of Technology, 2015.

[27] D. Degani and M. Tobak, Experimental study of controlled tip disturbance effect on flow asymmetry, Phys. Fluids A **4**, 2825 (1992).

[28] D. Degani, Effect of splitter plate on unsteady flows around a body of revolution at incidence, Phys. Fluids A **3**, 2122 (1991).

[29] D. Degani, L. B. Schiff, and Y. Levy, Numerical prediction of subsonic turbulent flows over slender bodies at high incidence, AIAA J. **29**, 2054 (1991).

[30] D. Degani and Y. Levy, Asymmetric turbulent vortical flows over slender bodies, AIAA J. **30**, 2267 (1992).

[31] D. Degani and L. B. Schiff, Numerical simulation of the effect of spatial disturbances on vortex asymmetry, AIAA J. **29**, 344 (1991).

[32] D. Degani, Instabilities of flows over bodies at large incidence, AIAA J. **30**, 94 (1992).

[33] S. M. Murman, Geometric perturbations and asymmetric vortex shedding about slender pointed bodies, in *Atmospheric Flight Mechanics Conference* (AIAA, Reston, VA, 2000), Paper-00-410.

[34] S. M. Murman, Vortex filtering for turbulence models applied to crossflow separation, in *39th Aerospace Sciences Meeting and Exhibit* (AIAA, Reston, VA, 2001), Paper-01-0114.

[35] K. Gee, R. M. Cummings, and L. B. Schiff, Turbulence model effects on separated flow about a prolate spheroid, AIAA J. **30**, 655 (1992).

[36] D. Degani, Effect of geometrical disturbance on vortex asymmetry, AIAA J. **29**, 560 (1991).

[37] L. B. Schiff, R. M. Cummings, R. L. Sorenson, and Y. Rizk, Numerical simulation of high-incidence flow over the f-18 fuselage forebody, J. Aircraft **28**, 609 (1991).

[38] P. J. Lamont, Pressures around an Inclined ogive cylinder with laminar, transitional, or turbulent separation, AIAA J. **20**, 1492 (1982).

[39] D. Degani, M. Tobak, and G. G. Zilliac, Surface flow patterns on an ogive-cylinder at incidence, AIAA J. **30**, 272 (1992).

[40] P. Lamont, The complex asymmetric flow over a 3.5D ogive nose and cylindrical afterbody at high angles of attack, in *AIAA 20th Aerospace Sciences Meeting* (AIAA, Reston, VA, 1982), Paper-82-0053.

[41] G. G. Zilliac, D. Degani, and M. Tobak, Asymmetric vortices on a slender body of revolution, AIAA J. **29**, 667 (1991).

[42] P. Dexter, A study of asymmetric flow over slender bodies at high angles of attack in a low turbulence environment, in *22nd Aerospace Sciences Meeting* (AIAA, Reston, VA, 1984), Paper-84-0505.

[43] Y. Levy, D. Degani, and A. Seginer, Graphical visualization of vortical flows by means of helicity, AIAA J. **28**, 1347 (1990).

[44] S. E. Ramberg, The effects of yaw and finite length upon the vortex wakes of stationary and vibrating circular cylinders, J. Fluid Mech. **128**, 81 (1983).

[45] L. Mi and O. Gottlieb, Asymptotic model-based estimation of a wake oscillator for a tethered sphere in uniform flow, J. Fluids Struct. **54**, 361 (2015).

[46] O. O'Reilly and P. J. Holmes, Non-linear, nonplanar and nonperiodic vibrations of a string, J. Sound Vib. **153**, 413 (1992).

[47] M. B. Rubin and O. Gottlieb, Numerical solutions of forced vibration and whirling of a nonlinear string using the theory of a cosserat point, J. Sound Vib. **197**, 85 (1996).

[48] L. Mi and O. Gottlieb, Stabilization of a multi-tethered lighter-than-air rigid-body sphere undergoing vortex-induced vibrations in uniform flow, Nonlinear Dyn. **93**, 1353 (2018).

[49] C. H. K. Williamson and R. Govardhan, Vortex-induced vibrations, Annu. Rev. Fluid Mech. **36**, 413 (2004).

[50] J. Zhao, K. Hourigan, and M. C. Thompson, Dynamic response of elliptical cylinders undergoing transverse flow-induced vibration, J. Fluids Struct. **89**, 123 (2019).

[51] N. Jauvtis, R. Govardhan, and C. H. K. Williamson, Multiple modes of vortex-induced vibration of a sphere, J. Fluids Struct. **15**, 555 (2001).

[52] R. van Hout, A. Krakovich, and O. Gottlieb, Time resolved measurements of vortex-induced vibrations of a tethered sphere in uniform flow, Phys. Fluids **22**, 087101 (2010).

[53] M. M. Rajamuni, M. C. Thompson, and K. Hourigan, Transverse flow-induced vibrations of a sphere, J. Fluid Mech. **837**, 931 (2018).